Synergistic osteogenic and angiogenic effects of KP and QK peptides incorporated with an injectable and self-healing hydrogel for efficient bone regeneration

Runze Li [a,1], Chen Zhou [a,1], Jun Chen [b,c,d,1,*], Haotian Luo [a], Ruoyu Li [a], Danying Chen [a], Xuenong Zou [d,**], Weicai Wang [a,***]

[a] Hospital of Stomatology, Guanghua School of Stomatology, Guangdong Provincial Key Laboratory of Stomatology, Sun Yat-sen University, 56 Lingyuanxi Road, Guangzhou, 510055, China
[b] Department of Organ Transplantation, Zhujiang Hospital, Southern Medical University, Guangzhou, 510280, China
[c] The Key Laboratory of Imflammation and Autoimmune Diseases, Guangzhou, 510280, China
[d] Guangdong Provincial Key Laboratory of Orthopaedics and Traumatology, Department of Spine Surgery, The First Affiliated Hospital, Sun Yat-sen University, Guangzhou, 510080, China

ARTICLE INFO

ABSTRACT

Irregular defects generated by trauma or surgery in orthopaedics practice were usually difficult to be fitted by the preformed traditional bone graft substitute. Therefore, the injectable hydrogels have attracted an increasing interest for bone repair because of their fittability and mini-invasivity. However, the uncontrollable spreading or mechanical failures during its manipulation remain a problem to be solved. Moreover, in order to achieve vascularized bone regeneration, alternatives of osteogenic and angiogenic growth factors should be adopted to avoid the problem of immunogenicity and high cost.

In this study, a novel injectable self-healing hydrogel system (GMO hydrogel) loaded with KP and QK peptides had been developed for enhancing vascularized regeneration of small irregular bone defect. The dynamic imine bonds between gelatin methacryloyl and oxidized dextran provided the GMO hydrogel with self-healing and shear-thinning abilities, which led to an excellent injectability and fittability. By photopolymerization of the enclosed GelMA, GMO hydrogel was further strengthened and thus more suitable for bone regeneration. Besides, the osteogenic peptide KP and angiogenic peptide QK were tethered to GMO hydrogel by Schiff base reaction, leading to desired releasing profiles. *In vitro*, this composite hydrogel could significantly improve the osteogenic differentiation of BMSCs and angiogenesis ability of HUVECs. *In vivo*, KP and QK in the GMO hydrogel demonstrated a significant synergistic effect in promoting new bone formation in rat calvaria. Overall, the KP and QK loaded GMO hydrogel was injectable and self-healing, which can be served as an efficient approach for vascularized bone regeneration via a minimally invasive approach.

1. Introduction

Bone defects resulting from trauma, infection, tumor or chronic inflammation cause severe physical and psychological harm to the patients. Reconstruction and repair of the critical bone defects is still challenging, especially for those residing deep with irregular shapes [1–3]. Over the past decades, a large number of biomaterial-based approaches for bone regeneration have been proposed with desirable

outcomes, however, a majority of these required extensive surgical exposure before implantation and usually failed in fitting the irregular bone defects in practice [4]. The urgent need of mini-invasive and shape-adaptable bone regeneration strategies encourage the development of next-generation of bioactive materials. Among these, hydrogels have attracted an increasing attention due to their ability to mimic extracellular matrix (ECM) by providing a hydrophilic three-dimensional microenvironment suitable for endogenous cell growth [5].

Injectable hydrogels represent a family of materials that can be easily processed into the desired area under light forces (normally less than 100 N) [6]. Traditional injectable hydrogels were produced based on "sol-gel" transition strategy, which indicated that these hydrogels maintained liquid form during extrusion from the syringe. Subsequently, a solid gel was formed after injection with time or by external stimulus, such as heat and pH [7,8]. So far, a lot of injectable hydrogels based on "sol-gel" transition strategies had been successfully proposed. However, the gelation processes were hard to process and injection failure occurred occasionally. For instance, some injectable hydrogels had a restricted manipulation time, which mainly depends on the gelation process [9]. Too rapid gelation of the hydrogel indicated a limited manipulation time, which could increase the probability of clogging within the needle. Although delaying the gelation or initiating gelation after injection could gain a sufficient manipulation time [10], the liquid-form materials incline to disperse before solidification, thus, causing an undesirable losing of hydrogel and spreading of the drugs/-cells after injection. Therefore, developing novel strategies for hydrogels that can pass smoothly through the needle of syringe and retain *in situ* without spreading is worth exploring. Dynamic covalent bonds are capable in endowing the hydrogels with the self-healing and shear-thinning ability, which can serve as a novel strategy to fabricate injectable hydrogel [11]. Hydrogels with self-healing and shear-thinning properties exhibit reversible "gel-sol" transition due to the natural reversible bond breaking and reforming, thus, making them ideal scaffolds to deliver the cells or drugs via injection. In this case, the injectable hydrogels formed by the dynamic covalent bonds can retain the gel-form prior to injection and undergo a gel-sol transformation upon shear loading during injection. After injection, these hydrogels can rapidly integrate and self-heal *in situ* to prevent the post-transplantation dispersal [12–14].

Bone repair is a complex and orchestrated process in which propriate angiogenesis and osteogenesis play critical roles. How to achieve sufficient and rapid vascularization is a critical concern while designing bone regenerative materials [15]. As widely known, bone morphogenetic proteins (BMPs) [16] and vascular endothelial growth factor (VEGF) [17] are used as osteoinductive and angiogenic factors to enhance bone regeneration, respectively. Recently, an increasing number of studies have revealed that delivering BMPs and VEGF together can result in the synergistic outcomes with respect to promoting the new bone formation [18–20]. However, application of growth factors in practice had some drawbacks, such as high costs of production, immunogenicity and transient effect owing to their short half-life and unstable structure [21, 22]. With the development of the synthetic techniques, peptide drugs have been considered as a promising alternative for the growth factors. The peptides can be easily synthesized and modified in a cost-effective manner by using the liquid- or solid-phase synthesis procedures. Due to their small size, the peptides were more stable and less likely to elicit an immune response [23–25]. Previous studies have proven that peptide corresponding to sequence in the knuckle epitope of BMP2 possessed osteogenic activities [26], whereas a peptide corresponding to the helix sequence of VEGF had been used to regulate angiogenesis [27]. Loading both angiogenic and osteogenic peptides into bone regenerative scaffolds is promising in vascularized bone regeneration.

In this study, a novel injectable and self-healing hydrogel system (referred to as GMO hydrogel) has been developed to stimulate bone regeneration and reconstruction by sustained release of both angiogenic and osteogenic peptides. The first network of this injectable GMO hydrogel was formed by Schiff base reaction between the amino groups of GelMA and aldehyde groups of ODex. The single network hydrogels possessed excellent shear-thinning and rapid self-healing ability, which guaranteed their injectable and *in-situ* self-healing performance. In order to avoid rapid degradation and to acquire sufficient mechanical strength for bone regeneration, a secondary reinforced network was introduced in the matrix via photopolymerization of GelMA. Furthermore, osteogenic peptide (KP) and angiogenic peptide (QK), which were designed from BMP2 and VEGF respectively, were tethered to the hydrogel via Schiff base reaction for the first time to achieve desirable release profiles. Subsequently, the osteogenic/angiogenic performance and bone regeneration efficiency of the injectable composite hydrogel were comprehensively investigated *in vitro* and *in vivo*. (Scheme 1).

2. Materials and methods

2.1. Materials

Dextran, NaIO$_4$, β-glycerol phosphate, dexamethasone, ascorbate-2-phosphate, cetylpyridinium chloride (CPC), Triton X-100, para-formaldehyde and crystal violet were purchased from Sigma-Aldrich (MO, USA). Methacrylate gelatin (GelMA, EFL-GM-60, 60% graft degree), lithium phenyl-2,4,6-trimethylbenzoylphosphinate (LAP) and GelMA lysis kit (EFL-GM-LS-001) were supplied by Suzhou Intelligent Manufacturing Research Institute (Suzhou, China). The methacrylate gelatin was further characterized by ^{1}H NMR (Fig. S1). The BMP2 knuckle epitope derived peptide (KP) (N to C sequence: KIPK(Ac) ASSVPTELSAISTLYL), FITC labeled KP (N to C sequence: KIPK(Ac) ASSVPTELSAISTLYL-FITC), VEGF derived peptide (QK) (N to C sequence: KLTWQELYQLK(Ac)YK(Ac)GI) and TAMRA labeled QK (N to C sequence: KLTWQELYQLK(Ac)YK(Ac)GI-TAMRA) were commercially synthesized and identified by ChinaPeptides Co. Ltd. (Shanghai, China). α-MEM medium, fetal bovine serum (FBS), GlutaMAX™, penicillin/streptomycin, D-PBS and PBS were procured from Gibco BRL (NY, USA). Alizarin red staining kit, oil red staining kit, alcian blue staining kit, adipogenic and chondrogenic differentiation medium were purchased form Cyagen Biosciences lnc. (Suzhou, China). iFluor™ 488-phalloidin, Hoechst33324, BCA protein assay and anti-rabbit secondary antibodies were supplied by Beyotime Biotechnology (Shanghai, China). RIPA lysis buffer, protease and phosphatase inhibitors, TBST and bovine serum albumin (BSA) were provided by CoWin Biosciences (Nanjing, China).

2.2. Synthesis of ODex and GMO hydrogels

Oxidized dextran (ODex) was synthesized according to a previously reported method [28]. In brief, 3% NaIO$_4$ solution (w/v) was added to 5% dextran solution (w/v) dropwise, followed by stirring in dark for 3 h. After adding an equimolar amount of diethylene glycol to quench the unreacted NaIO$_4$, the ODex solution was dialyzed exhaustively and subsequently lyophilized at −80 °C. The obtained ODex foam was kept at −20 °C prior to use. The synthesized ODex was characterized by ^{1}H NMR and FTIR spectra (Fig. S2). The oxidation degree of dextran was determined by quantifying the unreacted aldehyde groups after reacting with tert-bytylcarbazate (TBC) [28]. The oxidation degree of dextran was determined to be 35.6%.

GelMA and LAP were dissolved in the PBS solution at 50 °C (with a final concentration of 10% and 0.25% w/v). Afterwards, the solution was mixed with the ODex solution at final concentrations as 1% (w/v). After incubating at 37 °C for 30 min, the single network GMO hydrogel (SN-GMO) were facilely obtained. The double-network GMO hydrogels (DN-GMO) could be further fabricated after being exposed to 405 nm light for 90 s (25 mW/cm^2). For the peptide loaded GMO hydrogel, the KP or/and QK peptide solutions were mixed with the ODex solution in advance, then the GelMA and LAP solutions were added subsequently. The solution containing 10% (w/v) GelMA and 0.25% (w/v) LAP was
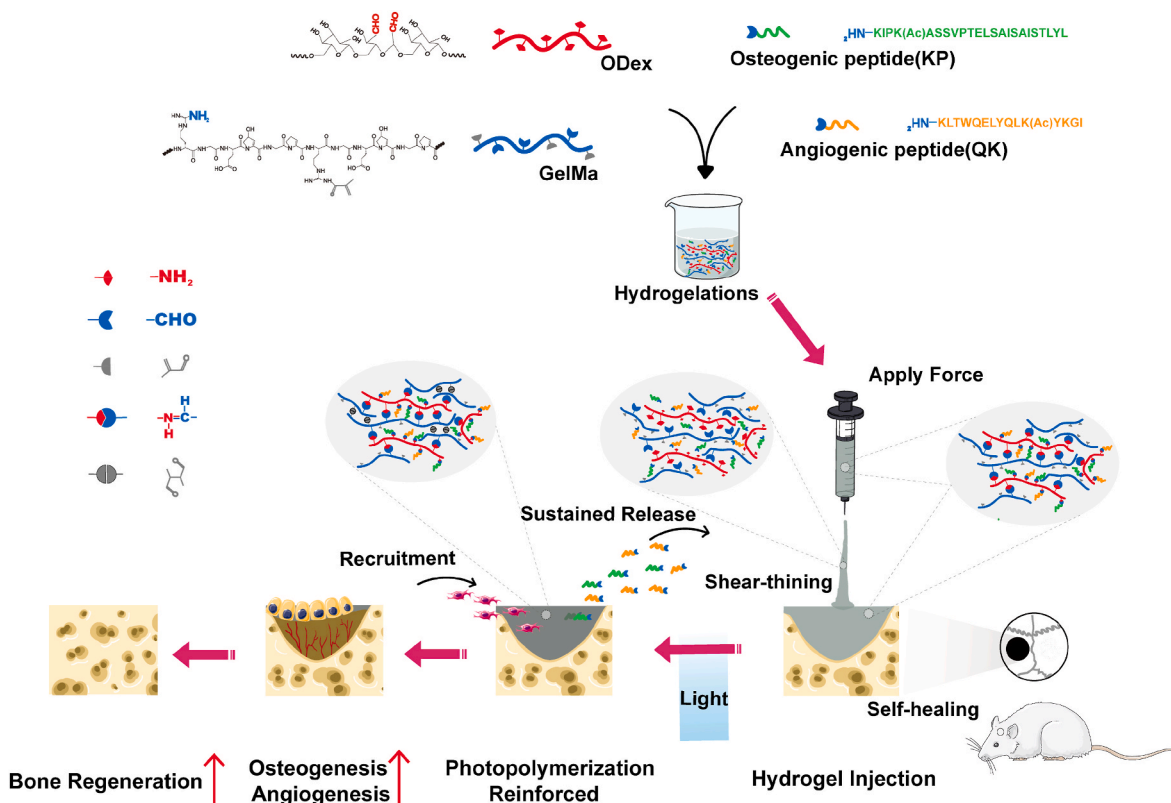
Scheme 1. Schematic illustration of this study. GMO hydrogel loaded with osteogenic (KP) and angiogenic (QK) peptides could be injected into the defect area of rat calvaria bone (based on its shear-thinning and self healing properties), sustainedly releasing of both bioactive peptides and recruiting of surrounding cells, thus, synergistically promote vascularized bone regeneration.

exposed to 405 nm light for 90 s (25 mW/cm^2) to obtain GelMA hydrogel.

2.3. Characterization of GMO hydrogels

FTIR analysis: Fourier transformed infrared (FTIR) spectra of Odex, GelMA, and GMO were measured by NICOLET 6700 FTIR spectrameter (Thermo, US) in a range of 4000-550 cm^{-1}.

Rheological analysis: The rheological measurements were performed by using an AR-G2 rheometer (TA Instruments). The time-sweep oscillatory tests were carried out immediately after loading the mixture of the hydrogel precursors at 0.5% strain and 1 Hz frequency to monitor the gelation process of the hydrogels. After the hydrogels were stabilized, the frequency-sweep tests were carried out from 1 to 100 rad/s at 0.5% strain and 1 Hz frequency. To quantitatively evaluate the self-healing capability of the hydrogels, the hydrogels were first damaged by increasing the strain from 0.5% to 200% at 1 Hz, and the self-healing behavior was subsequently monitored via the time-sweep test upon decreasing the strain to 0.5%.

Scanning electron microscopy (SEM): The hydrogels were loaded on the copper grids after freeze drying. Afterwards, the samples were sprayed with gold and characterized by using a scanning electron microscope (FEI QUANTA200, Czech) with an acceleration voltage of 10 kV.

Compressive analysis: The compressive stress-strain analysis of SN-GMO hydrogel, GelMA hydrogel (10% w/v), DN-GMO hydrogel and DN-GMO hydrogel loaded with KP and QK were conducted by using a universal testing machine (Instron E3000, UK). For this purpose, the hydrogels were prepared in the form of cylinders with 13 mm in diameter and 5 mm in height. The compressive analysis was performed up to 80% of the original height with a steady strain rate of 1 mm/min.

Swelling and enzymolysis assay: The cylinderical hydrogels (13 mm

in diameter, 3 mm in height) were prepared as described above. To evaluate swelling ratio of the hydrogels, the initial weights (M_0) were measured first. Subsequently, the hydrogels were immersed in PBS solution (pH = 7.4). At different points, the weight of the wet samples (M_t) was measured. The swelling ratio of the hydrogels was calculated according to the following equation: $W_t = (M_t - M_0)/M_0 \times 100\%$. To evaluate the enzymolysis of the hydrogels, the initial weights (M_0) were measured first. Afterwads, the hydrogels were immersed in PBS solution (pH = 7.4) containing 1 mg/mL collagenase I (Sigma-Aldrich, USA). The collagenase solution was replaced every 12 h to maintain the enzyme activity. At different points, the weight of the wet samples (M_t) was measured. The percent residual mass of the sample was calculated according to the following equation: residual mass% = $M_t/M_0 \times 100\%$. All experiments were conducted in triplicate.

2.4. Peptides releasing profiles

KP-FITC, QK-TAMRA, ODex, GelMA and LAP were dissolved in PBS. Subsequently, the KP-FITC and QK-TAMRA solutions were mixed with the ODex solution respectively and incubated at 37 °C for 30 min. The GelMA and LAP solutions were added next, and the prehdyrogel was obtained with the final KP-FITC concentrations of 500 μg/mL and QK-TAMRA concentrations of 300 μg/mL 1.5 mL hydrogel were photo-crosslinked by using the visible light (405 nm, 25 mW/cm^2) and then immersed with 4 mL PBS in a 15 mL centrifuge tube. 100 μL supernatant was collected at different time intervals (1, 3, 6, 9, 12, 15,18, 21 d). Further, 100 μL fresh PBS was added to the incubation mixture. The concentration of KP or QK in the collected PBS was determined by estimating the fluorescence intensity of FITC (Ex:492 nm, Em: 518 nm) and TAMRA (Ex:542 nm, Em: 568 nm), respectively, by using a micro-plate spectrophotometer (Bio-Tek, UK). The fluorescence intensity of FITC or TAMRA in 4 mL PBS containing 750 μg KP-FITC or 450 μg QK-

TAMRA was denoted as the total fluorescence intensity. The releasing profiles were determined from the ratio between the supernatant and total fluorescence intensity.

2.5. Isolation, identification and cultivation of BMSCs

Isolation, identification and cultivation of the bone marrow mesenchymal stem cells (BMSCs) were carried out by following the reported protocols [29,30]. In specific, the femurs and tibias were isolated from the C57/BL6 mice (4–6 weeks of age) after cervical dislocation. After flushing with a syringe, bone marrow cells were cultured with the complete α-MEM medium (containing 15% FBS, 1% v/v GlutaMAX™ and 1% v/v penicillin/streptomycin) at 37 °C in a 5% CO_2 humidified cell culture incubator. The adherent cells were collected and passaged, with the cells from passages 2 to 3 (P2-3) used for the subsequent experiments. The medium was changed every 2–3 days during culturing.

A phase-contrast microscope (Zeiss, Germany) was used to image BMSCs after reaching 90% confluency. The multiple differentiation ability of BMSCs was confirmed by the alizarin red, oil red and alcian blue staining after 21 days culturing in different induction mediums. The surface markers of BMSCs were analyzed by flow cytometry (Beckman CytoFLEX, USA) based on CD29, CD34, CD44, CD45 and CD90.2 (BioLegend, USA).

2.6. Acquisition and cultivation of HUVECs

Human umbilical vein endothelial cells (HUVECs) were purchased from ScienCell™ Reserch Laboratories (USA) and cultured in the Endothelial Cell Medium (ECM) containing 5% FBS, 1% v/v penicillin/streptomycin and 1% ECGS (purchased from ScienCell™ Reserch Laboratories, USA) at 37 °C in a 5% CO_2 humidified cell culture incubator. The cells from passages 2 to 5 (P2-5) were used for the subsequent experiments.

2.7. Cell viability, proliferation and spreading assessment

The CCK-8 cell proliferation assay was performed as per the manufacturer's instructions. Specifically, BMSCs and HUVECs were planted in the 48-well plates alone or palates covered with different hydrogels at a density of 1×10^4 cells/well. The medium was removed after 1, 3, 5 and 7 days of incubation, and a fresh culture medium containing 10% v/v Cell Counting Kit-8 (CCK-8, Dojindo Molecular Technologies Inc., Japan) was added to the 48-well plates, followed by incubation for 1 h at 37 °C in a 5% CO_2 humidified cell culture incubator in the absence of light. Subsequently, 100 μL supernatant medium was transferred to the 96 well plates, and the absorbance at a wavelength of 450 nm was measured using a microplate spectrophotometer (Bio-Tek, UK).

The live/dead staining assay was performed by using the LIVE/DEAD assay kit (Invitrogen, USA), following the manufacturer's instructions. BMSCs and HUVECs were planted in the 48-well plates alone or palates covered with different hydrogels at a density of 2×10^4 cells/well. Calcein AM and ethidium homodimer-1 were diluted in D-PBS to form the staining solution with concentrations of 2 μM and 4 μM, respectively. Subsequently, the staining solution was added to the well after removing the culture medium and incubated for 30 min at 37 °C in a 5% CO_2 humidified cell culture incubator in the absence of light. The live (green stain, Ex:480 nm, Em: 530 nm) and dead (red stain, Ex:530 nm, Em: 645 nm) cells were imaged using an inverted fluorescence microscope (Zeiss, Germany).

The immunofluorescent staining with iFluor™ 488-phalloidin and Hoechst33342 was performed by following the manufacturer's instructions. Briefly, BMSCs and HUVECs were planted in the 35 mm confocal dishes alone or confocal dishes covered with different hydrogels at a density of 1×10^5 cells/dish. The cells were fixed in 4% paraformaldehyde and permeabilized with the PBS solution containing 1% Triton X-100. Afterwards, the cells were stained with phalloidin for

1 h and Hoechst for 5 min at room temperature. Finally, the cells were imaged by using a laser scanning confocal microscope (Olympus, Japan).

2.8. Osteogenic induction, alkaline phosphatase staining, alizarin red staining and quantification of BMSCs

The osteogenic induction medium (OM) was obtained by adding 10 mM β-glycerol phosphate, 100 nM dexamethasone and 50 mg/mL ascorbate-2-phosphate in the culture medium. The OM medium was changed every 3 days during the osteogenic differentiation of BMSCs. The GelMA lysis kit and trypsin were used to decompose the hydrogels and acquire cells on the hydrogels.

The alkaline phosphatase (ALP) staining was conducted by using the Alkaline Phosphatase Staining Kit (Yeasen, China), following the manufacturer's instructions. Briefly, BMSCs were fixed by 4% paraformaldehyde (PFA), followed by washing with the PBS and staining for 30 min after osteogenic induction. The stained cells were imaged by using a phase-contrast microscope (Zeiss, Germany). Meanwhile, to evaluate the alkaline phosphatase (ALP) activity of BMSCs, the cell lysates were characterized using the ALP activity measurement kit (Jiancheng Nanjing, China). After incubation with the *p*-nitrophenyl phosphate solution, the alkaline phosphatase activity was calculated by measuring the absorbance at 520 nm with a microplate spectrophotometer (Bio-Tek, UK).

The Alizarin Red S solution was used to stain the deposited calcium in BMSCs after osteogenic induction. Briefly, BMSCs were fixed by 4% PFA, followed by staining by using the Alizarin Red S solution at room temperature for 30 min and washing with PBS. The cells were characterized by using a phase-contrast microscope (Zeiss, Germany). 10% cetylpyridinium chloride (CPC) was used to dissolve the stained calcium deposition, and the absorbance was measured at 562 nm using a microplate spectrophotometer (Bio-Tek, UK) for the determining the mineralization.

2.9. Tube formation and migration ability assessments of HUVECs

The Matrigel (BD Biosciences, USA) was used for evaluating the tube formation ability of HUVECs. After thawing on ice overnight, 250 μL Matrigel was added to the 48 well plates, followed by incubation at 37 °C for 30 min for gelation. HUVECs were planted on the Matrigel at a concentration of 2.5×10^4/well with different treatments (the leaching media were obtained by soaking the corresponding hydrogels for 72 h). The cells were subsequently incubated at 37 °C with 5% CO_2 for 6 h. Afterwards, the cells were imaged by using a phase-contrast microscope (Zeiss, Germany). The quantification analysis was performed by using the ImageJ software.

A 8.0 μm pore Transwell (BD Falcon™, USA) system was used to evaluate the migration of HUVECs. HUVECs were trypsinized and resuspended, followed by loading in the upper chamber at a density of 2×10^5/insert. Different hydrogels were placed in the lower chamber. After 24 h, the cells were fixed with 4% paraformaldehyde for 30 min and subsequently stained with 0.1% crystal violet. The migrated cells (at the bottom surface of the insert) were imaged by using a phase-contrast microscope (Zeiss, Germany).

A linear wound scratch model was used to assess the migration of HUVECs as well. HUVECs were seeded at a density of 2×10^5 cells/well in the 12 well plates and allowed to grow to 100% confluency. After starving for 3 h, a linear scratch (approximate 600 μm wide) was introduced in the monolayer, and the cells were incubated at 37 °C and 5% CO_2 for 12 h with different leaching media (serum-free). Afterwards, the cells were imaged by using a phase-contrast microscope (Zeiss, Germany). The relative closure of the scratch wound was quantified by measuring the wound area with the ImageJ software.

2.10. Quantitative real-time PCR

The gene encoding runt-related transcription factor 2 (RUNX2), Osterix (OSX), alkaline phosphatase (ALP), Osteopontin (OPN) and osteocalcin (OCN) of BMSCs were determined by employing the quantitative real-time PCR analysis. After osteogenic stimulation, total RNA was extracted from the cells with TRIzol (Thermo, USA) and reverse transcribed into cDNA using the HiScript® III 1st Strand cDNA Synthesis Kit (Vazyme, China), following the manufacturer's instructions. The quantitative real-time PCR was performed by using the AceQ qPCR SYBR Green Master Mix (Vazyme, China) under the following thermocycling conditions: 95 °C for 5 min, 40 cycles at 95 °C for 20 s, 60 °C for 30 s and 72 °C for 30s. The primer sequences are shown in Table S1. *Gapdh* was used as an internal control for PCR. The relative expression of genes was calculated using the $2^{-\Delta\Delta Ct}$ method.

The gene encoding platelet endothelial cell adhesion molecule or CD31 (PECAM1), von Willebrand factor (VWF) and plasmalemma vesicle-associated protein (PLVAP) of HUVECs were determined by employing the quantitative real-time PCR as well. After culturing on different hydrogels, total RNA was extracted from the cells with TRIzol and reverse transcription, and the quantitative real-time PCR was conducted as previously mentioned. The primer sequences are shown in Table S1.

2.11. Western blot analysis

After osteogenic stimulation, the total protein of BMSCs was extracted by the RIPA lysis buffer supplemented with 1% protease and phosphatase inhibitors. Afterwards, the protein concentration was determined by using the BCA protein assay. Next, the proteins were resolved by SDS-PAGE (Genscript, China) and transferred to a polyvinylidene fluoride (PVDF) membrane (Millipore, USA) by using a wet transfer blotting system (Bio-Rad, China). The membranes were placed in a blocking solution (TBST containing 5% non-fat dry milk) for 1 h. Subsequently, the membranes were incubated at 4 °C overnight with appropriate primary antibodies: monoclonal rabbit anti-RUNX2 (1:1000, CST, USA), polyclonal rabbit anti-ALP (1:1000, Abcam, USA) and polyclonal rabbit anti-β-Actin (1:1000, Servicebio, China). Afterwards, the membranes were washed and incubated with the relevant secondary antibodies (1:10000) for 1 h at room temperature. The band signals were detected using the ECL western blotting substrate kit (Millipore, USA). The relative intensities of each immunoreactive band were quantified by using the ImageJ software.

After starving for 6 h, HUVECs were treated with different leaching mediums (ECGS-free) for 30 min. The subsequent procedure was the same as mentioned earlier. The primary antibodies used for analysis were: monoclonal rabbit anti-Phospho-p44/42 MAPK (Erk1/2) (1:2000, CST, USA), monoclonal rabbit anti-p44/42 MAPK (Erk1/2) (1:1000, CST, USA), monoclonal rabbit anti-Phospho-Akt (1:2000, CST, USA), monoclonal rabbit anti-Akt (1:1000, CST, USA) and polyclonal rabbit anti-β-Actin (1:1000, Servicebio, China).

2.12. Immunofluorescence

BMSCs were cultivated on different hydrogels with the osteogenic medium. Afterwards, the cells were washed with the PBS solution and fixed with 4% paraformaldehyde for 15 min. After incubation with 0.5% TBST for 30 min, the cells were blocked in the PBS solution containing 5% BSA for 30 min. Next, the cells were incubated with the primary antibodies anti-RUNX2 (1:200, CST, USA) and anti-OPN (1:200 Abcam, USA) overnight at 4 °C. Subsequently, the secondary antibodies conjugated to FITC were incubated at room temperature for 1 h. Finally, the nucleus was stained with Hoechst33342. The cells were characterized using a laser scanning confocal microscope (Zeiss, Germany).

2.13. Animal surgery

All animal procedures were approved by the Institutional Animal Care and Use Committee (IACUC) of Sun Yat-Sen University (Reference: SYSU-IACUC-2021-000445). Eight-week-old male SD rats, weighing 250–300 g, were used in this study. The rats were randomly divided into four groups: (1) DN-GMO hydrogel alone (GMO Ctrl group); (2) DN-GMO hydrogel with QK (QK/GMO group); (4) DN-GMO hydrogel with KP (KP/GMO group); and (5) DN-GMO hydrogel with KP and QK (KP/QK/GMO group). The final concentration of the incorporated KP and QK was 500 μg/mL and 300 μg/mL respectively. The rats were anesthetized with 1% pentobarbital (0.4 mL/100 g) via the intraperitoneal injection. After cleaning and sterilizing the skin, a longitudinal incision of approximately 2 cm in length was made to cut the skin and subcutaneous tissue. Next, the circular full-thickness bone defects of 5 mm in diameter was made by an electric trephine drill. The corresponding hydrogels were subsequently implanted in the defect area va injection. After filling of the defect area, hydrogels were exposed to 405 nm light for 90 s (25 mW/cm^2) for reinforcement. The soft tissue and skin were then sutured layer by layer carefully. After 8 weeks, the rats were euthanized to harvest the cranial bone. The tissues were fixed in 4% paraformaldehyde solution for 24 h and stored in 75% ethanol for subsequent analysis.

2.14. Micro-CT analysis

After harvesting the samples, each sample was scanned using a micro-CT system at 70 kV and 114 μA (Scanco Medical μCT 50, Switzerland). The results were reconstructed and analyzed by using a data analysis software (Avizo 8.1, USA). The region of interest was set to be a 5-mm circle along the defect edge and was subsequently used to calculate the ratio of the bone volume (BV) to the total volume (TV) for quantitatively assessing the bone formation.

2.15. Histological analysis and immunohistochemistry (IHC)

After micro-CT analysis, the samples were decalcified in ethylene diamine tetraacetic acid (EDTA) for 6 weeks. After dehydration by graded alcohol series and embedding in paraffin, the samples were cut into 6-μm sections for staining. The sections were stained with hematoxylin & eosin (H & E) and Masson's trichrome stain according to the manufacturer's protocol (Servicebio, China). As for immunohistochemistry, after dewaxing, rehydration and antigen retrieval, the slices were incubated overnight with anti-OPN (1:200, Abcam, USA), anti-CD31 (1:200, Servicebio, China) primary antibodies at 4 °C. After incubation with the appropriate secondary antibodies for 1 h at room temperature, diaminobenzidine (DAB) (Servicebio, China) was used for visualization, followed by counterstaining with hematoxylin (Servicebio, China). The Aperio AT2 slide scanner (Leica Biosystems, Germany) was used for imaging the tissue slices. The IHC-Toolbox plugin (NIH, USA) of ImageJ was used to quantify the immunohistochemistry images.

2.16. Statistical analysis

The data was expressed as mean ± standard deviation (SD) of at least three independent experiments. The comparisons were performed by using the GraphPad Prism software. Statistical analysis was performed by employing the Student's two-tailed *t*-test or one-way analysis of variance (ANOVA). The differences between groups or treatments were reported as ns/Ns (non-significant) or significant (*$P < 0.05$, **$P < 0.01$, ***$P < 0.001$ vs Ctrl; #$P < 0.05$, ##$P < 0.01$ and ###$P < 0.001$ among groups).

3. Results

3.1. Fabrication and characterization of GMO hydrogels

The single-network GMO hydrogel (SN-GMO) was formed by mixing the pre-dissolved GelMA and ODex solution. As shown in Fig. 1A, after 30 min incubation at 37 °C, the prehydrogel solution changed from a liquid to a gel with a light-yellow appearance, while the prehydrogel containing only GelMA was still liquid before photopolymerization (Fig. 1B). Then the FTIR spectra of GelMA, ODex, SN-GMO and double-network GMO hydrogel (DN-GMO) were measured. As shown in Fig. 1C, the characteristic peak at 1730 cm^{-1} corresponding to carbonyl stretching of ODex almost disappeared in the spectrum of SN-GMO and DN-GMO, while the peak band at 1542 cm^{-1} attributed to the primary amino group exhibited decreased intensity in spectrum of SN-GMO and DN-GMO than GelMA, indicating the consumption of aldehyde group of ODex and primary amino group of GelMA, respectively [31,32]. In addition, the –N═C- characteristic peak at 1644 cm^{-1} present in the SN-GMO and DN-GMO spectrum, suggesting Schiff base was formed via

the reaction of aldehyde group and amino group [33]. The slight decrease of amide II peak at 1534 cm-1 in spectrum of DN-GMO compared with SN-GMO indicate reaction between methacryloyl groups during light irradiation [34].

Gelation time was characterized by rheometer via the time sweep analysis. At the physiological temperature, SN-GMO hydrogel was formed via Schiff base reaction (Fig. 1D). Besides, as shown in the frequency sweep results, the G′ values keeps higher than the corresponding G'' values in the range of 1–100 Hz, demonstrating that stable structure was formed via the first network (Fig. 1E).

The mechanical behavior was further tested by compressive analysis. As shown in Fig. 1F and G, the SN-GMO hydrogel had a relatively flat curve and low compression modulus (4.5 ± 0.7 kPa), while the DN-GMO hydrogel exhibited the typical "J-shaped" stress-strain curves and presented a much higher compression modulus (136.5 ± 11.6 kPa). It indicated that introducing the covalent bonds in the dynamic hydrogel could significantly improve its mechanical strength. The compression modulus of the DN-GMO hydrogel was also higher than the GelMA hydrogel (87.7 ± 7.9 kPa), which signaled that the Schiff base formed in
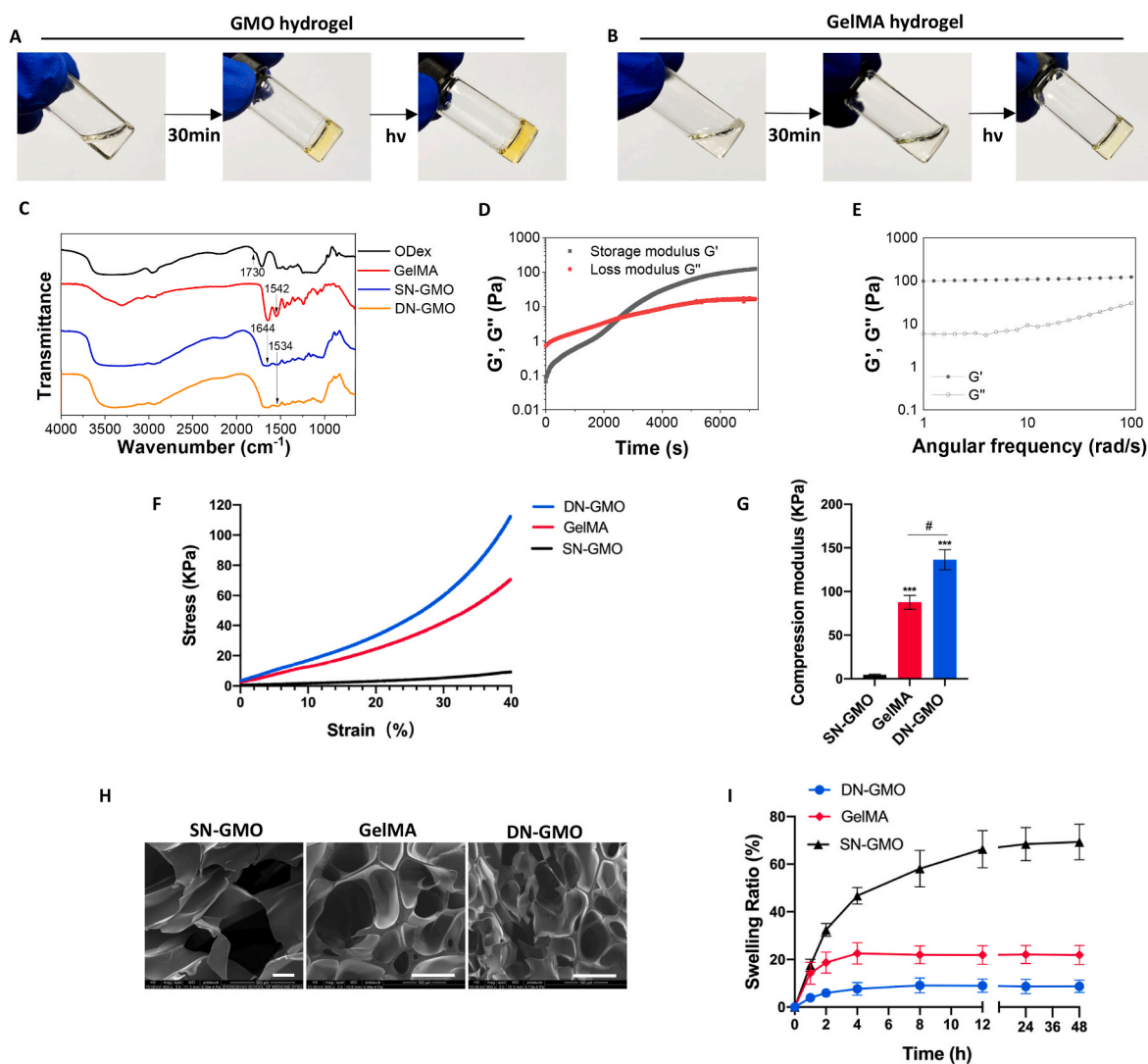
Fig. 1. Fabrication and characterization of GMO hydrogels.
(A) Optical images of GMO hydrogel and **(B)** GelMA hydrogel formation. **(C)** FTIR spctra of ODex, GelMA, SN-GMO hydrogel (SN-GMO) and DN-GMO hdyroel (DN-GMO). **(D)** Time sweep of G′ and G'' of the SN-GMO hydrogel after mixing; **(E)** Frequency sweep of SN-GMO hydrogel. **(F)** Stress-strain curves and **(G)** compressive modulus of GelMA, SN-GMO and DN-GMO hydrogel at 25 °C. **(H)** SEM images of GelMA, SN-GMO and DN-GMO hydrogel. Scale bar = 100 μm. **(I)** Swelling ratio of the GelMA, SN-GMO and DN-GMO hydrogel in PBS at 37 °C. (n = 3; $^{NS}P>0.05$, $^*P < 0.05$, and $^{**}P < 0.01$, $^{***}P < 0.001$ compared with Ctrl group; $^{ns}P>0.05$, $^\#P < 0.05$, and $^{\#\#}P < 0.01$, $^{\#\#\#}P < 0.001$ compared among groups).

the GMO hydrogel could also improve its mechanical strength. However, there was no statistical difference as compared with the DN-GMO hydrogel incorporated with or without peptides (Fig. S3C).

The microstructure of the hydrogels was examined by SEM. As shown in Fig. 1H and Fig. S3A, the DN-GMO and peptides incorporated DN-GMO hydrogel (KP/QK/DN-GMO) tended to present smaller pore size as compared with SN-GMO or GelMA, indicating a denser cross-linkings inside. Overall, the hydrogels presented porous microstructure which was suitable for nutrient exchange, cell attachment and proliferation [35,36]. Then the swelling ratios of GelMA, SN-GMO and DN-GMO hydrogel were studied. As shown in Fig. 1I, DN-GMO hydrogel presented the lowest swelling ratio (9.1 ± 3.1%) compared with GelMA hydrogel (21.9 ± 3.8%) and SN-GMO hydrogel (69.3 ± 7.5%). This indicated that introducing dynamic covalent bond can enhance the network density and decrease the swelling rate of hydrogels. Rapid increment of volume due to absorbing water from surrounding may accelerate degradation of the hydrogel. As shown in Fig. S4, the three gelatin based hydrogel (SN-GMO, GelMA and DN-GMO) were sensitive to collagenase and could be completely decomposed with 1 mg/mL concentration. However, the DN-GMO showed a delayed enzymolysis process. The decreased swelling ratio and degradation rate improved the mechanical stability and morphological compatibility of the DN-GMO hydrogel. .

3.2. Dynamic properties and release profile of GMO hydrogels

To verify the self-healing capability of the SN-GMO hydrogel, the bulk hydrogels stained with TAMRA (Red) and FITC (yellow) were cut into two halves, respectively. By replacing the two halves of the hydrogel together, the gap were observed to diminish gradually and a complete integration was observed after incubation at 37 °C for 30 min (Fig. 2A). Furthermore, step-strain measurements were carried out to quantitatively evaluate the repetitive self-healing ability of the hydrogels (Fig. 2B). When the loading strain increased from 0.5% to 200%, the crossover of G′ and G″ with a sharp reduction in the former one and an increment in the latter one, indicating the structural destruction of the hydrogel networks and the transition from the "gel" to "sol" behavior. Then the hydrogels rapidly transformed from the "sol" to "gel" character and recovered their original modulus while the loading strain was decreased to 0.5%. As shown in Fig. 2B, the recovery rate and extent of the SN-GMO hydrogel barely changed after several cycles, demonstrating the repetitive self-healing capability of the hydrogel.

The steady-shear measurement result revealed that the hydrogels displayed an excellent shear-thinning behaviors, evidenced by the sharp decreasing of viscosity upon increasing of the shear rate (Fig. 2G). Then the self-healing and shear-thinning behavior of hydrogels with different ODex concentration were studied. As shown in Fig. S5, on increasing the ODex concentration, the healing time and efficiency of the hydrogels were decreased. For practical applications, the ideal injectable hydrogel should integrate and recover the mechanical strength once injected at the target site [37]. The rapid self-recovery of structural and mechanical properties guarantee the spontaneous integration of the hydrogel after injection and repair the mini cracks during usage. Therefore, GMO hydrogel containing 1% Odex was chosen in this study for subsequent experiment. Then the SN-GMO hydrogel was tested by injecting through a 26G syringe. The specific written shapes stranded on the glass sides immediately after injection neither spreading nor leakage (Fig. 2E and F). Meanwhile, the SN-GMO hydorgel could also be injected into water without any breakage (Fig. 2D). These results indicated that the SN-GMO hydrogel had the potency to be implanted mini-invasively via injection, which can significantly reduce the surgery exposures during the bone defect restoration.

Bioactive peptides QK and KP were tethered to the hydrogel matrix through imine bonds formed via the reaction between aldehyde groups of ODex and primary amino groups of peptides. Peptides with fluorescence labels were used to study the release profile of the GMO hydrogels. As shown in Fig. 2H, a constant and sustained release of KP and QK was observed up to 21 d in the DN-GMO hydrogels. In contrast, a burst release was observed in GelMa hydrogels (Fig. 2I), which released over 70% peptides in 3 days and almost 90% in 7 days. The sustained
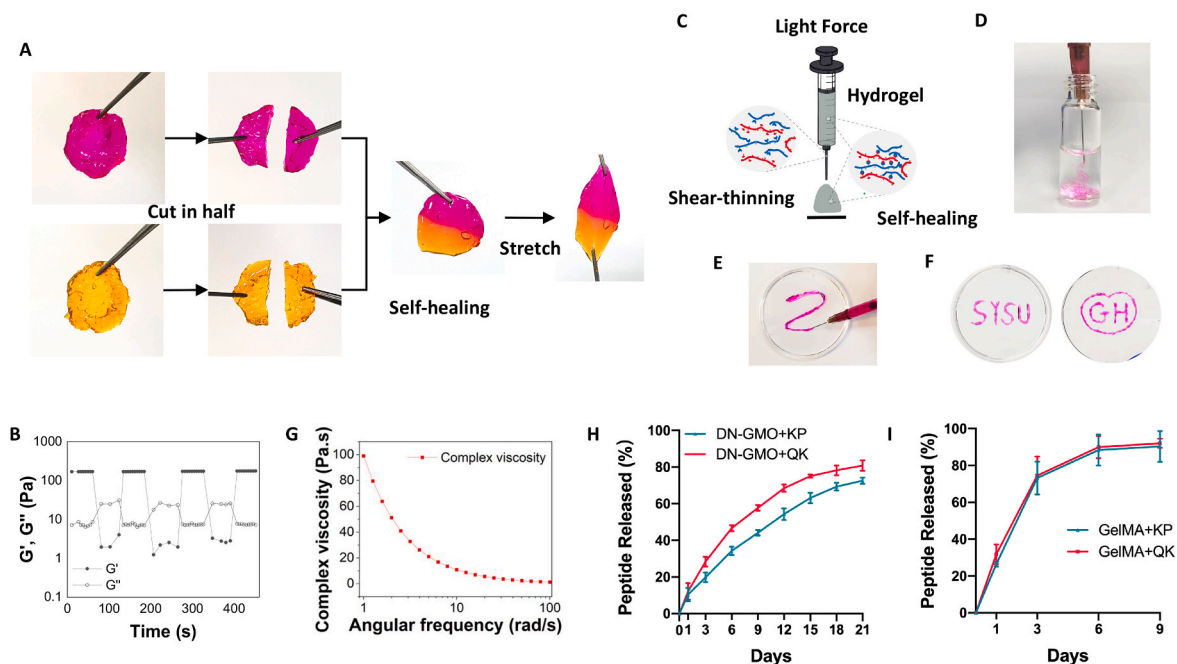
Fig. 2. Assessment of the dynamic properties and peptide release profile of GMO hydrogels.
(A) Optical images of the self-healing process of the SN-GMO hydrogel. **(B)** Four-cycle step-strain measurement of the SN-GMO hydrogel at strain from 0.5% to 200% at 1 Hz. **(C)** Schematic illustration of the injection process for the SN-GMO hydrogel. **(D)** Optical images of the SN-GMO hydrogel injected into water or **(E)** on glass side. **(F)** Optical images of the SN-GMO hydrogel written into "SYSU" and "GH" on glass side through injection. **(G)** Complex viscosity changes of SN-GMO hydrogel in frequency sweeps from 1 to 100 rad/s at 0.5% strain and 1 Hz frequency. **(H)** Peptides releasing profiles from DN-GMO hydorgel and **(I)** GelMA hydrogel.

releasing profile of the osteogenic and angiogenic peptides further guaranteed the biological function of the hydrogel.

3.3. Cytotoxicity assessment of the GMO hydrogels

The biocompatibility is a crucial assessment for biomaterials [5,38, 39]. To assess the cytotoxicity of the composite GMO hydrogels *in vitro*, BMSCs and HUVECs were used for the subsequent experiments. BMSCs were characterized for their morphology (Fig. S6A), multilineage

differentiation abilities (Figs. S6B–D) and cell surface markers (Fig. S6E) before used. In advance, the concentrations of the incorporated KP and QK peptides were optimized *in vitro*. The ALP activity (Fig. S7A) and *Ostrix* expression (Fig. S7B) of BMSCs were elevated with the increase of KP concentration from 0 to 500 μg/mL, however, no difference was observed on increasing the KP concentration from 500 to 700 μg/mL. Similarly, the expression of *PLVAP* (Fig. S7C) and the activation of MAPK(ERK1/2) pathway (Figs. S7D–6F) of HUVECs were elevated on increasing the QK concentration from 0 to 300 μg/mL. However, there
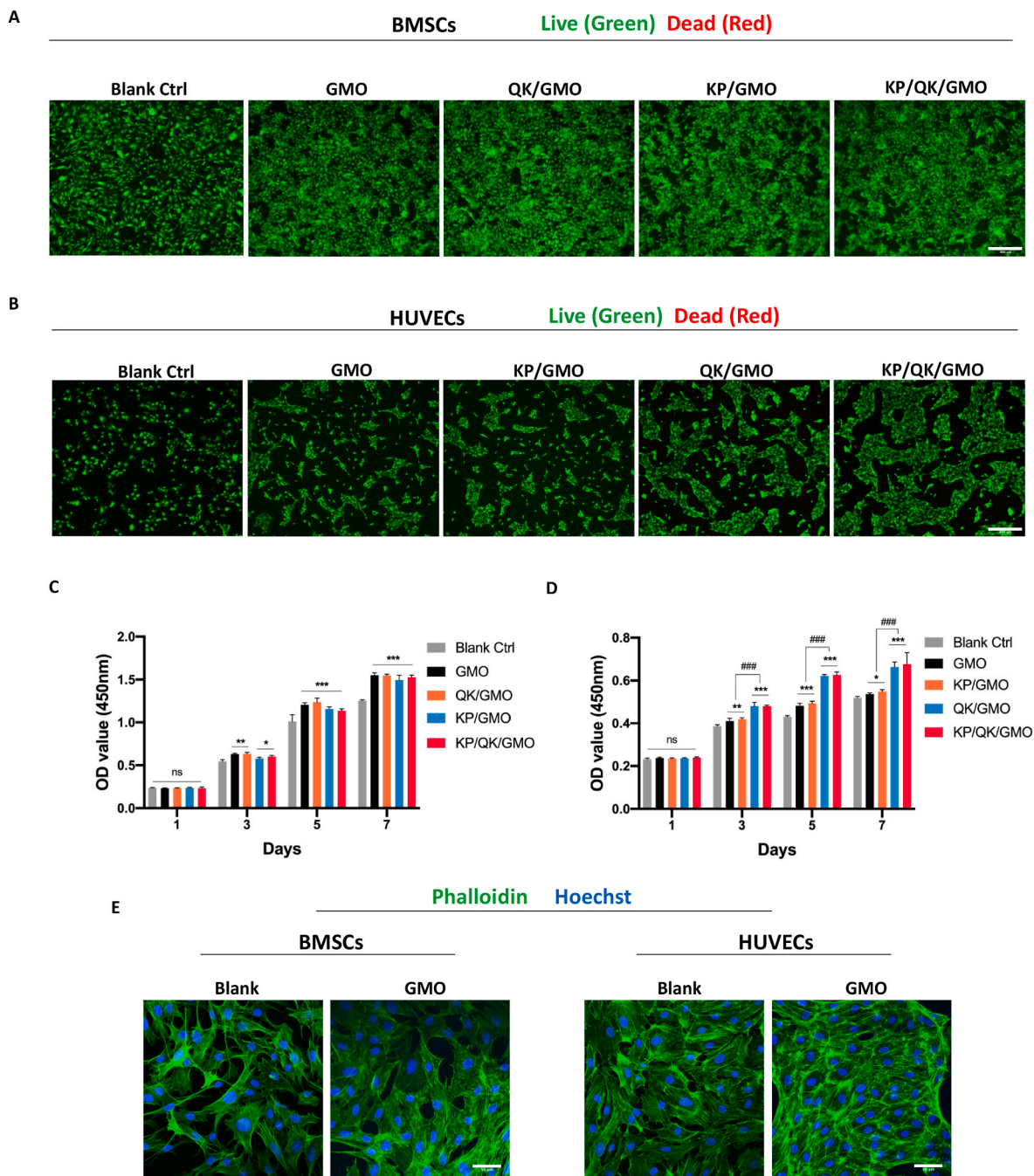
Fig. 3. Cytotoxicity assessment of the composite GMO Hydrogels.
(A) Representative live-dead images of BMSCs and **(B)** HUVECs that were seeded on the glass dishes (Blank Ctrl), DN-GMO hydrogel alone (GMO) and with KP (KP/GMO), QK (QK/GMO), KP + QK (KP/QK/GMO) incorporated respectively. Scale bar = 400 μm. Live: green; Dead: read. **(C)** CCK-8 assay of BMSCs and **(D)** HUVECs cultivated on glass dishes (Blank Ctrl), the DN-GMO hydrogel alone (GMO) and with KP (KP/GMO), QK (QK/GMO), KP + QK (KP/QK/GMO) incorporated respectively after 1, 3, 5, and 7 days of seeding. **(E)** Representative images of cytoskeleton and nucleus staining images of BMSCs (Left) and HUVECs (Right) cultivated on the glass dishes (Blank) and DN-GMO hydrogel (GMO) after 24 h. Scale bar = 50 μm. (n = 3; $^{NS}P>0.05$, $*P < 0.05$, and $**P < 0.01$, $***P < 0.001$ compared with Ctrl group; $^{ns}P>0.05$, $^{#}P < 0.05$, and $^{##}P < 0.01$, $^{###}P < 0.001$ compared among groups).

were no significant differences on enhancing the QK concentrations from 300 to 400 μg/mL. Therefore, the GMO hydrogels containing 500 μg/mL KP and 300 μg/mL QK were used for futher study.

To directly observe the cell viability, the live/dead staining was carried out to stain BMSCs and HUVECs cultivated without hydrogels (Blank Ctrl), on the DN-GMO hydrogel alone (GMO) as well as the hydrogels incorporated with QK (QK/GMO), KP (KP/GMO) or KP + QK (KP/QK/GMO). As expected, BMSCs (Fig. 3A) and HUVECs (Fig. 3B) on the hydrogels exhibited a high viability after seeding, and almost no dead cells were detected. The CCK-8 assay was further used to evaluate the survival and proliferation of BMSCs and HUVECs. The cell proliferation was analyzed at the duration of 1, 3, 5 and 7 d. As shown in Fig. 3C, the OD values in all groups increased with time, thus, suggesting that the GMO hydrogel did not show any toxicity on the cells. Moreover, from 3 days onwards, the OD value in all four hydrogel groups was higher than the Blank Ctrl group, which indicated that GMO hydrogels could enhanced the cell proliferation activity. As for HUVECs, the OD values for all hydrogels were observed to increase with time (Fig. 3D), which suggested that the GMO hydrogel exhibited cytocompatibility for the cultivated HUVECs as well. Interestingly, from 3 days onwards, the OD value for the QK/GMO and QK/KP/GMO groups were significantly higher than the GMO group, which indicated an accelerated proliferation of HUVECs in these groups. As the OD values of the KP/GMO and GMO groups were similar, the observed improvement in the proliferation was mainly attributed to the presence of QK. It is well established that VEGF can significantly increased the proliferation of ECs for angiogenesis [40]. The observed results indicate that QK also presents a high growth promotion effect on HUVECs, which is beneficial for further vascular tissue formation.

Meanwhile, to verify the adhesion and spreading of the cells, the skeleton and nucleus of BMSCs and HUVECs cultivated without hydrogel and on the DN-GMO hydrogel were stained 24 h after seeding. As shown in Fig. 3E, the cells spread well on the surface of the DN-GMO hydrogel, thus, suggesting the healthy status. The obtained results indicated that the GMO hydrogel alone or loaded with the bioactive peptides exhibited a high cell compatibility.

3.4. Promotion of osteogenic differentiation of BMSCs in vitro by KP loaded GMO hydrogels

To further verify the osteoinductivity, the ALP and ARS staining assays were first conducted to analyze the early and late osteogenic differentiation of BMSCs on different hydrogels. The ALP staining results (Fig. 4A) demonstrated that BMSCs in the KP/GMO and QK/KP/GMO groups presented a more ALP-positive area and a higher staining intensity than the GMO group after 7 days. The ALP activity assay of the cell lysates revealed the similar results (Fig. 4B). As for the ARS staining, the results (Fig. 4C) indicated a dramatic improvement in the calcium nodule formation in the KP/GMO and QK/KP/GMO groups after 21 days. It could be further verified by the semi-quantitative analysis of the mineralized nodules (Fig. 4D). Next, the expression of the early and late osteogenic markers of the hydrogel groups were detected by qPCR. As shown in Fig. 4E, the expression of *Runx2, Osterix and Alpl* in BMSCs was significantly upregulated after culturing on the DN-GMO hydrogels loaded with KP or KP/QK peptide for 7 days, whereas *Opn and Ocn* was significantly upregulated after 14 days. Meanwhile, the osteogenic-relative protein expression of BMSCs cultivated on different GMO hydrogels was detected after 7 days. The western Blot results (Fig. 4F) indicated that the selected proteins (RUNX2 and ALP) were ungulated in the KP/GMO or KP/QK/GMO groups as compared with the other groups. The quantitative analysis based on the band density (Fig. 4G) further confirmed the obtained results. To observe the RUNX2 and OPN expression of BMSCs cultivated on different GMO hydrogels directly, the immunofluorescence staining was further conducted. As expected, the immunofluorescence staining presented similar expression pattern as the mRNA and proteins mentioned earlier. BMSCs in the KP/GMO and

KP/QK/GMO groups exhibited a higher RUNX2 fluoresce intensity in the nucleus after 7 days and a higher OPN fluoresce intensity mainly in the cytoplasm after 14 days (Fig. 4H). However, there were no statistical differences in the ALP activity, calcium nodule formation and osteogenic gene expression between the QK/GMO and GMO Ctrl groups, the KP/GMO and KP/QK/GMO groups also expressed no statistical differences. Generally, KP in the hydrogels played a key role in promoting osteogenesis of BMSCs. The observed results indicated that the KP loaded GMO hydrogel revealed an excellent osteoindutive ability *in vitro* by upregulating the expression of the osteogenic proteins and genes.

3.5. Stimulation of angiogenesis of HUVECs in vitro by QK loaded GMO hydrogels

The angiogenic functions of the composite GMO hydrogels with HUVECs were further explored. First, the migration of HUVECs was examined by the transwell migration and scratch wound assays. The transwell migration assay (Fig. 5A) revealed that the released peptides from the QK/GMO and QK/KP/GMO groups could significantly increase the migration of HUVECs as compared with the GMO Ctrl group. The quantitative analysis of the number of the migrated cells (Fig. 5B) was consistent with the observation. Meanwhile, the scratch wound assay also indicated that the DN-GMO hydrogels loaded with QK or QK and KP could significantly accelerate the migration of HUVECs to the wound area (Fig. 5C), thus, resulting in an enhanced healing ratio (Fig. 5D) as compared with the DN-GMO hydrogel alone. These observed results verified that the QK loaded GMO hydrogel significantly promoted the migration of the endothelial cells. Next, the tube formation ability of HUVECs treated by the released peptides from different hydrogels was further measured. The QK/GMO and QK/KP/GMO groups showed a markedly improvement of the branch points (Fig. 5F) and total length (Fig. 5G) of the tubes formed by HUVECs on the Matrigel, which presented a superior tubular morphology than the GMO Ctrl group (Fig. 5E). Furthermore, the activation of the several pro-angiogenesis pathways was evaluated by Western Blot. As shown in Fig. 5H and I, the released peptides from the QK/GMO and QK/KP/GMO groups significantly promoted the phosphorylation of ERK1/2 and AKT, thus, indicating the activation of the MAPK(ERK1/2) and PI3K/Akt pathways. The quantitative analysis (Fig. 5J and K) of the proteins, their respective phosphorylated form and ratio based on the band density further confirmed the observation results. Finally, the expression of genes involving the cell-cell interactions and endothelial function of HUVECs cultivated on different hydrogels after 3 days were analyzed. As shown in Fig. 5L, an obvious upregulation of *PLVAP, VWF and PECAM1* was observed in the QK/GMO and QK/KP/GMO groups as compared with the GMO Ctrl group. However, any significant effect of KP in promoting the angiogenesis of HUVECs was not observed.

The obtained results indicated that the QK loaded GMO hydrogel exhibited an excellent pro-angiogenic ability *in vitro* by activating the angiogenic pathways and promoting the expression of the angiogenesis related genes.

3.6. Synergistically enhanced critical bone repair in vivo by GMO hydrogels loaded with KP and QK

The bone regenerative capacities of the hydrogels were explored by using the critical-sized calvaria bone defect models in the rats. Eight-week-old male Sprague Dawley rats were randomly divided into four groups (GMO Ctrl, QK/GMO, KP/GMO and QK/KP/GMO). After the critical-size defects were created, corresponding hydrogels were injected in the defect area (Fig. 6A). As shown in the three-dimensional reconstruction (Fig. 6C), only a few new bones were observed to be formed at the edges of the defect areas in the GMO Ctrl group. Compared with the GMO Ctrl group, the KP/GMO group exhibited an almost healed bone defect repair, which was consistent with the *in vitro* observations. Interestingly, the QK/GMO group also presented a superior efficiency of
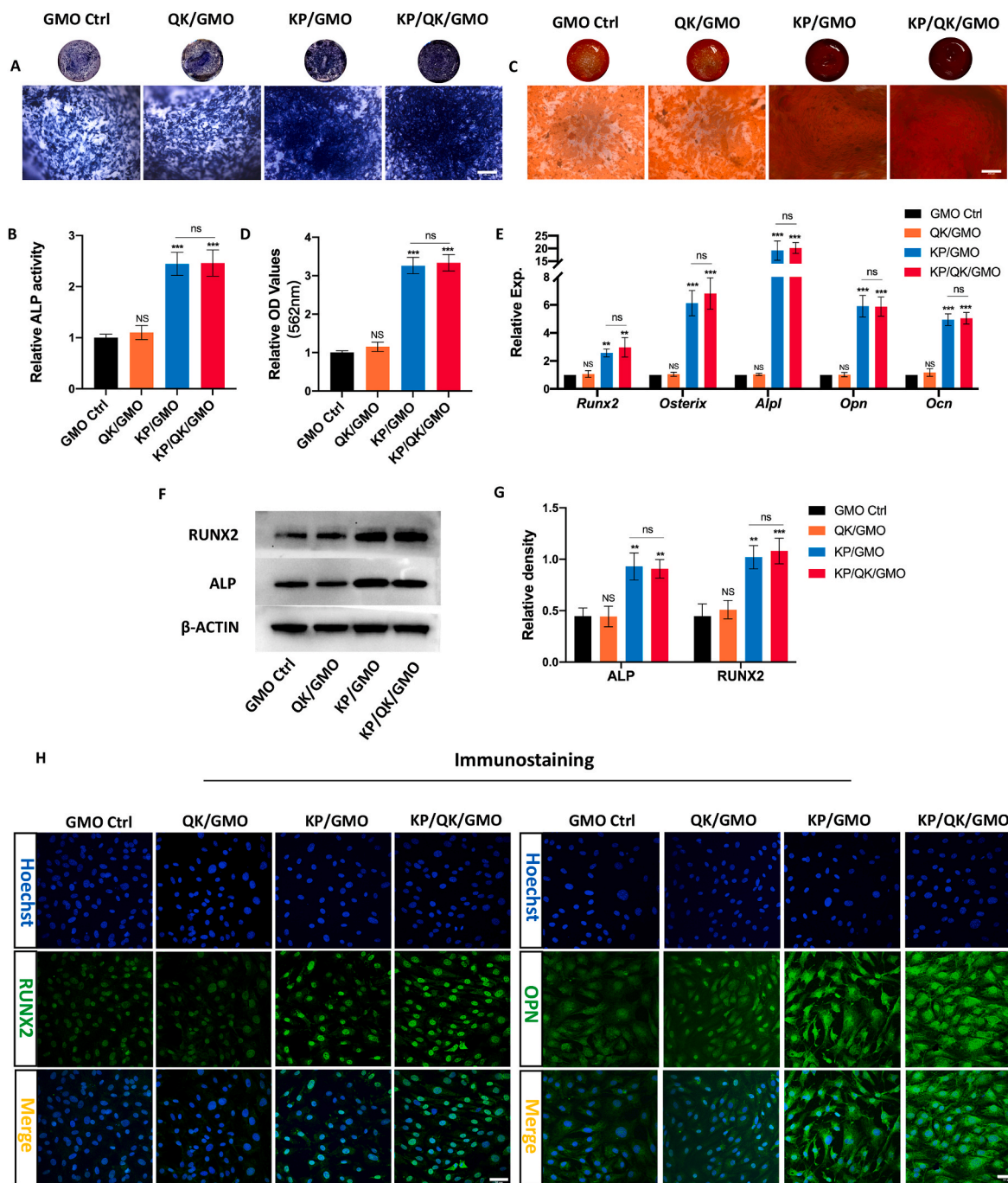
Fig. 4. Promotion of osteogenic differentiation of BMSCs *in vitro* by KP loaded GMO hydrogels.
(A) Representative images of gross appearance (upper) and microscopic images (lower) with ALP staining and **(B)** ALP activity of BMSCs cultivated on the DN-GMO hydrogel alone (GMO) and with KP (KP/GMO), QK (QK/GMO), KP + QK (KP/QK/GMO) incorporated after 7 days. Scale bar = 400 μm **(C)** Representative images of gross appearance (upper) and microscopic images (lower) with Alizarin red S staining of mineralized nodules and **(D)** semi-quantitative evaluation of Alizarin Red S staining of BMSCs cultivated on the DN-GMO hydrogel alone (GMO) and with KP (KP/GMO), QK (QK/GMO), KP + QK (KP/QK/GMO) incorporated after 21 days. Scale bar = 200 μm **(E)** qPCR analysis of osteogenic-related genes expression of BMSCs cultivated on the DN-GMO hydrogel alone (GMO) and with KP (KP/GMO), QK (QK/GMO), KP + QK (KP/QK/GMO) incorporated after 7 days (*Runx2, Osterix, Alpl*) and 14 days (*Opn, Ocn*). **(F)** Immunoblotted image for ALP, RUNX2 and β-ACTIN of BMSCs cultivated on the DN-GMO hydrogel alone (GMO) and with KP (KP/GMO), QK (QK/GMO), KP + QK (KP/QK/GMO) incorporated after 7 days. **(G)** Densitometric analyses of blots showing the values for ALP and RUNX2 proteins. **(H)** Representative immunofluorescent images for RUNX2 (Left) and OPN (Right) of BMSCs cultivated on the DN-GMO hydrogel alone (GMO) and with KP (KP/GMO), QK (QK/GMO), KP + QK (KP/QK/GMO) incorporated after 7 days and 14 days. RUNX2/OPN are marked by green fluorescence, and the cell nuclei were dyed blue by the Hoechst. Scale bar = 50 μm. (n = 3; $^{NS}P > 0.05$, $*P < 0.05$, and $**P < 0.01$, $***P < 0.001$ compared with Ctrl group; $^{ns}P > 0.05$, $^{\#}P < 0.05$, and $^{\#\#}P < 0.01$, $^{\#\#\#}P < 0.001$ compared among groups).
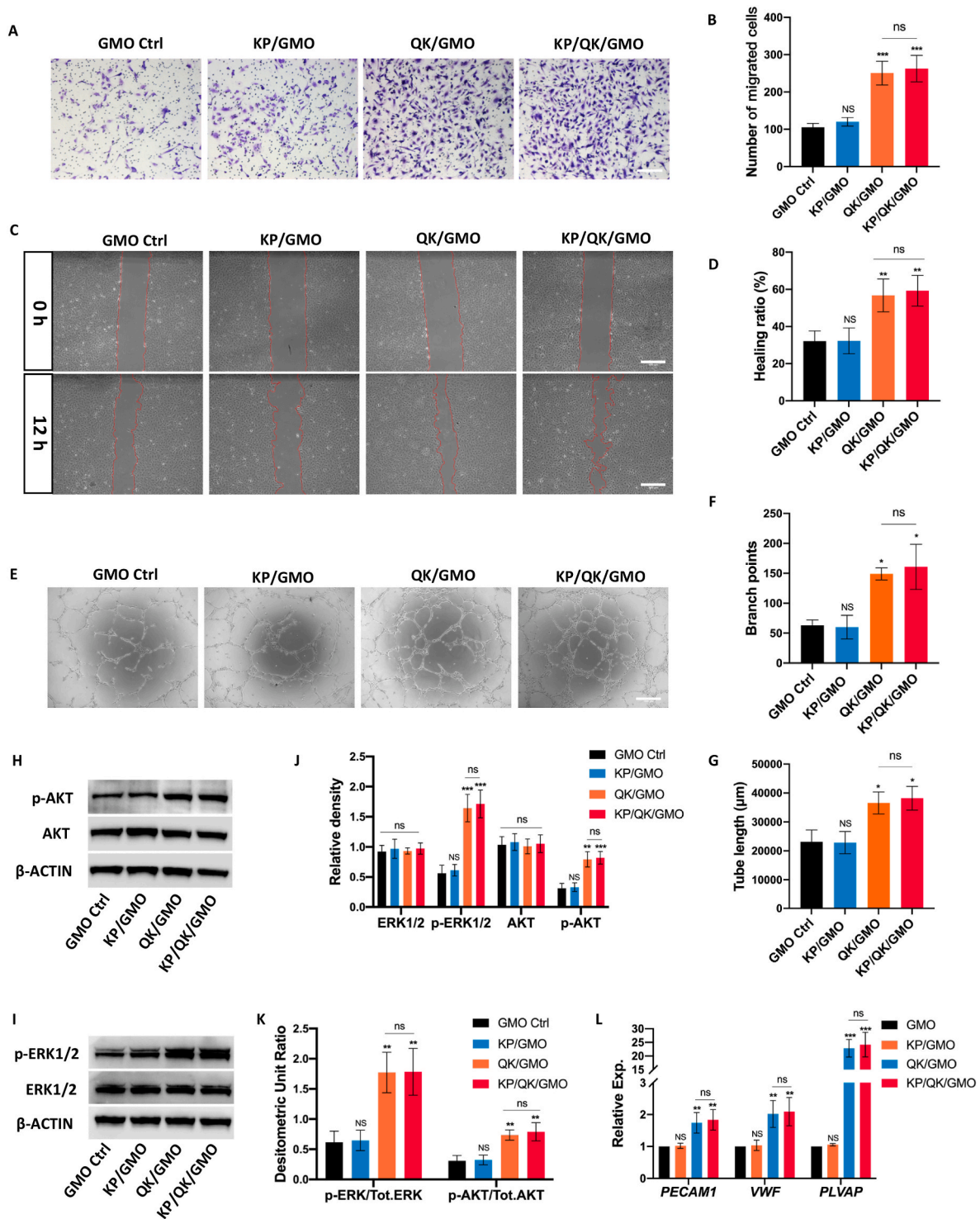
Fig. 5. Stimulation of angiogenesis of HUVECs *in vitro* by QK loaded GMO hydrogels.
(A) Representative microscopic images and **(B)** quantified numbers of the migrated HUVECs treated by released peptides from the DN-GMO hydrogel alone (GMO) and with KP (KP/GMO), QK (QK/GMO), KP + QK (KP/QK/GMO) incorporated in Transwell assay after 24 h. Scale bar = 200 μm **(C)** Representative microscopic images and **(D)** quantified analysis for the migrated HUVECs treated by released peptides from the DN-GMO hydrogel alone (GMO) and with KP (KP/GMO), QK (QK/GMO), KP + QK (KP/QK/GMO) incorporated in scratch wound healing assay (0 h, 12 h). Scale bar = 400 μm. **(E)** Representative microscopy images for the tube formation and quantitively analysis of **(F)** branch points, **(G)** tube lengths of HUVECs on Matrigel treated by released peptides from the DN-GMO hydrogel alone (GMO) and with KP (KP/GMO), QK (QK/GMO), KP + QK (KP/QK/GMO) incorporated after 6 h. Scale bar = 400 μm. **(H, I)** Immunoblotted image for *p*-ERK1/2, total ERK1/2, *p*-AKT, total AKT and β-ACTIN of HUVECs treated by released peptides from the DN-GMO hydrogel alone (GMO) and with KP (KP/GMO), QK (QK/GMO), KP + QK (KP/QK/GMO) incorporated. **(J)** Densitometric analyses of blots showing the values for phosphorylated and total protein of ERK1/2 and AKT **(K)** and the ratio between phosphorylated and total protein (densitometric unit ratio). **(L)** qPCR analysis of angiogenesis-related genes (*PECMA, VWF and PLVAP*) expression of HUVECs cultivated on the DN-GMO hydrogel alone (GMO) and with KP (KP/GMO), QK (QK/GMO), KP + QK (KP/QK/GMO) incorporated after 3 days. (n = 3; $^{NS}P > 0.05$, $^{*}P < 0.05$, and $^{**}P < 0.01$, $^{***}P < 0.001$ compared with Ctrl group; $^{ns}P > 0.05$, $^{\#}P < 0.05$, and $^{\#\#}P < 0.01$, $^{\#\#\#}P < 0.001$ compared among groups).
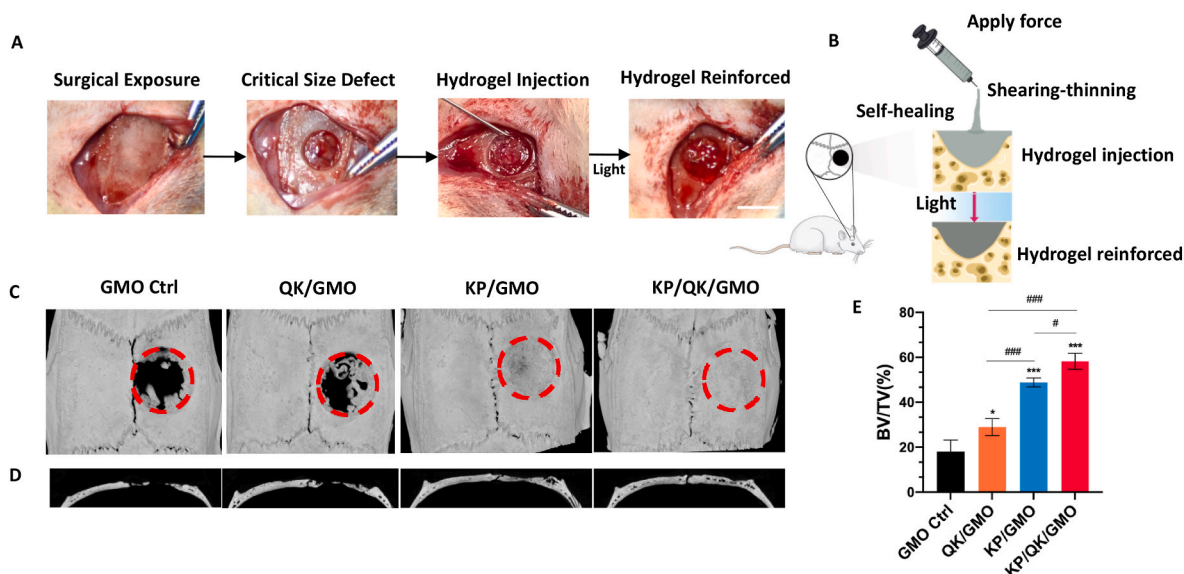
Fig. 6. **Synergistically enhanced of critical bone repair *in vivo* by GMO hydrogels loaded with KP and QK.**
(A) Gross images and **(B)** schematic illustration of the surgical procedures. Scale bar = 5 mm. **(C)** Representative images of 3D reconstruction and **(D)** sagittal crosssection showed the bone formation of the defect area treated with DN-GMO hydrogel alone (GMO Ctrl) or DN-GMO hydrogel with QK (QK/GMO), KP (KP/GMO) and KP + QK(KP/QK/GMO) incorporated after 8 weeks. **(E)** Quantitative analysis of bone formation by BV/TV in specific regions of interest. (n = 3–4; $^{NS}P > 0.05$, $^{*}P < 0.05$, and $^{**}P < 0.01$, $^{***}P < 0.001$ compared with Ctrl group; $^{ns}P > 0.05$, $^{#}P < 0.05$, and $^{##}P < 0.01$, $^{###}P < 0.001$ compared among groups).

bone repair as compared with the GMO Ctrl group, while the KP/QK/GMO group revealed the highest efficiency of bone repair among the groups. The sagittal crosssection images (Fig. 6D) were observed to be consistent with the reconstruction results. A consecutive regenerated bone was formed in the defect area in the KP/QK/GMO group, while the GMO Ctrl group only demonstrated a separated one. The other groups presented the behaviors in between the KP/QK/GMO and GMO Ctrl groups. As shown in the quantitative analyses of the BV/TV ratio (BV/TV × 100%) of the defect areas (Fig. 6E), compared with the low ratio (18.0 ± 5.2%) in the GMO Ctrl group, the BV fractions in the QK/GMO (28.9 ± 3.8%), KP/GMO (48.8 ± 2.0%) and KP/QK/GMO (58.2 ± 3.5%) groups were obviously increased, thus, indicating the accelerated bone bridging and defect reunion associated with the composite GMO hydrogels. Though QK had a limited effect on the osteogenic differentiation of BMSCs *in vitro*, however, it is worth noting that the QK loaded GMO hydrogel exhibited a slight promotion of the bone formation *in vivo*. Meanwhile, the GMO hydrogel with the incorporation of both KP and QK revealed a higher healing efficiency of the bone defects than those with KP alone, which indicated a synergistic effect of the two bioactive peptides *in vivo*.

The results of Hematoxylin & Eosin (H & E) and Masson's trichrome staining further confirmed the formation new bone in different groups. As shown in the H & E staining images (Fig. 7A), fibrous connective tissues were dominant in the defect areas, and there were only a few new bone formation in GMO Ctrl group. On the contrary, a large number of osseous tissues along the junction of the defects were observed in the KP/QK/GMO group, which led to a nearly complete healing. Moreover, the QK/GMO group also presented a superior new bone formation as compared with the GMO Ctrl group, while it was inferior as compared with the KP/GMO group. This was consistent with the microCT observation that the angiogenic peptide QK could also promote bone healing *in vivo*. Consistent with H & E staining, Masson's trichrome staining revealed that consecutive collagen fiber bundles and ossified tissues were arranged compactly in the defect area in the KP/QK/GMO group, while the GMO Ctrl group only demonstrated the connected fibers with a few new bone formation (Fig. 7B). The other groups presented the behaviors in between the KP/QK/GMO and GNO Ctrl groups. The results of the osteogenetic efficiency were further confirmed by immunohistochemical staining of OPN, which was expressed to the highest extent in

KP/QK/GMO group as well (Fig. 7C). The quantitative analysis of immunohistochemical staining revealed highest OPN expression in the KP/QK/GMO group, while there was only a slight expression in the GMO Ctrl group (Fig. 7E). In order to evaluate neovascularization in the bone defect area, the CD31 immunohistochemical staining was further performed (Fig. 7D). Compared with the GMO Ctrl group, only a slightly higher number of the newly formed vessels were noted in the KP/GMO group. However, more newly formed vessels were observed in the groups containing QK peptides. In particular, KP/QK/GMO group showed the highest number of vessels among all groups. The quantitative analysis of the number of vessels further confirmed the observed results (Fig. 7F).

Overall, the obtained results suggested the sustained release of KP and QK from the injectable GMO hydrogel scaffold could synergistically promote the osteogenesis and angiogenesis of bone tissue, which further led to an efficient vascularized bone regeneration in the defect areas.

4. Discussion

Repairing irregular or deep burr-hole bone defect (e.g. in oral and maxillofacial region) is still a huge challenge to traditional hydrogel scaffolds. Although 3D printing is promising in endowing the scaffolds a significant shape-fitness, the requirement of extensive surgical exposure limited its application [41,42]. To overcome this issue, the current study aimed to design an injectable hydrogel that could easily pass through the needle of a syringe and possess the stability to retain *in situ*. Although the traditional injectable hydrogels based on "sol-gel" transition strategy have drawn much attention in the past decade, they still lack a sufficient maneuverability in clinical application due to the defined operation time, complex manipulation process, uncontrollable spreading or mechanical weaknesses.

To overcome the obstacles, novel injectable and self-healing hydrogels based on dynamic crosslinks have attracted increasing attentions recently. For example, Ding et al. [37] reported an injectable and self-healing hydrogel possessed dynamic –C═C- double bond based on the Knoevenagel condensation (KC) reaction by mixing cyanoacetate- and benzaldehyde-modified dextran. Although rapid self-healing and excellent injectable properties were achieved in this study, the requirement of catalyst for the KC reaction and the complicated
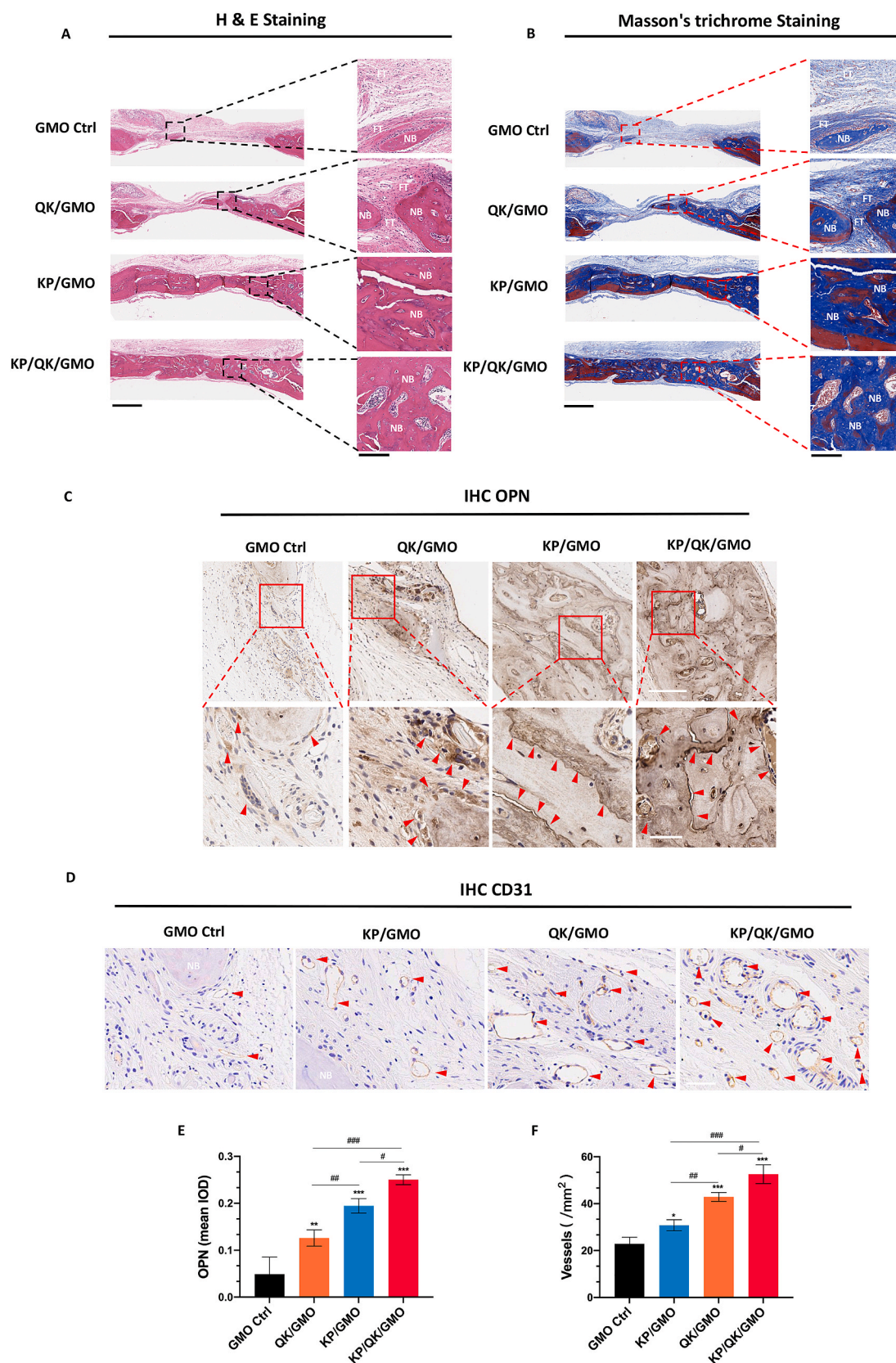
Fig. 7. Histological analysis of bone regeneration *in vivo*.
(A) Representative images of H & E and **(B)** Masson's trichrome staining for the defect area in each groups. Scale bar = 1 mm (Left); 200 μm (Right). NB: new bone; FT: fibrous tissues. **(C)** Representative immunohistochemical staining images of OPN and **(E)** the quantitative analysis in each group. Arrows point to the positive area. Scale bar = 200 μm (Upper); 50 μm (Lower). **(D)** Representative immunohistochemical staining images of CD31 and **(F)** the quantitative analysis of the vessels number in each group. Arrows point to the vessels. Scale bar = 50 μm. (n = 3–4; $^{NS}P>0.05$, $^*P < 0.05$, and $^{**}P < 0.01$, $^{***}P < 0.001$ compared with Ctrl group; $^{ns}P>0.05$, $^{\#}P < 0.05$, and $^{\#\#}P < 0.01$, $^{\#\#\#}P < 0.001$ compared among groups).

modifications of dextran increased the system complexity in this work. Another example was reported by Liu et al., where an injectable hydrogel based on 4-arm-thiolated polyethylene glycol (PEG-SH) and Mg^{2+} ions was developed [43]. Due to the reverse nature of the Mg–S coordination bond and disulfide bond, the formed hydrogel showed a promising shear-thinning property and could be extruded through a needle without any clogging. However, the synthetic polymers-based hydrogel may lack natural cell-targeting signals and need extra modifications to improve its biological responses in practice [44,45]. Therefore, developing injectable and self-healing hydrogels with a facile fabrication method and desirable biological responses is worth exploring. In our study, the hydrogel was synthesized mainly based on gelatin methacryloyl (GelMA) and oxidized dextran (ODex), which could be easily obtained by carrying out a slight modification of their original natural polymers. Considering the sufficient amino groups and aldehyde groups in the backbone of GelMA and Odex independently, the Schiff base, normally produced by the condensation reaction between the aldehyde groups and amines [12,46], was chosen to form the hydrogel network. As shown in Fig. 1, the first network of the GMO hydorgel could be facilely obtained by mixing precursors, the second network could be further formed after exposing to visible light. Due to the presence of RGD peptides and natural degradation sites for matrix metalloproteinases (MMPs) [47], the natural polymers-derived hydrogel displayed excellent biocompatibility and desirable biodegradability in our study (Fig. 3, Fig. S4).

The shear-thinning and self-healing properties are needed to be considered primarily when designing injectable hydrogels based on the "gel-sol-gel" transition strategy. The hydrogels with significant shear-thinning performance are expected to be injected with less forces. The rapid self-healing property further guarantees the spontaneous integration of the hydrogel after injection. Inappropriate design may lead to a reduction in the dynamic properties, thus, further altering the injectability of the hydrogel. For instance, the dynamic exchanges of the –C═C- double bond are relatively slow without a catalyst, therefore, the injectable hydrogel reported by Ding et al. displayed a reduced shear-thinning and self-healing properties without histidine and were not satisfactory as an injectable carrier [37]. In our study, the Schiff base displayed desirable dynamic properties under physiological condition without catalyst and endowed the GMO hydrogel with continuous and spontaneous self-healing ability (Fig. 2A and B) as well as a significant shear-thinning performance (Fig. 2G). There was no need to preform the material to match the shape of defects, and a minimal operative field exposure was guaranteed, which was advantageous in clinical practice. Interestingly, a bioadhesive hydrogel with high concentrations of GelMa (20%, w/v) and ODex (5%, w/v) was reported by Zhao et al. for sutureless keratoplasty [48]. Although the adhesive strength was greatly improved due to the high concentration of ODex, the hydrogel showed a limited "gel-sol-gel" transition performance in practice. Similarly, the self-healing efficiency of GMO hydorgel was decreased when increasing the Odex concentration in our study, which might further alter its injectability in practice. Therefore, a low concentration of ODex was used in the current study to obtain a self-healing and injectable hydrogel with excellent "gel-sol-gel" transition performance.

The ideal bone repair scaffolds should present sufficient structural stability and mechanical strength to frame the osteogenic environment, as the optimal hardness facilitate cell adhesion, proliferation and ultimately osteogenic differentiation [2,5,49]. Substantial injectable hydrogels based on the dynamic crosslinks had been proposed recently, but the low mechanical strength and rapid degradation hindered their application as bone restoration materials [6,50,51]. For example, Tseng et al. reported a dynamic hydrogel based on glycol chitosan and telechelic difunctional poly(ethylene glycol) (DFPEG) [52]. Due to the reversible Schiff base inside, the hydorgel showed a excellent self-healing and injectable ability, however, an insufficient stiffness (G' ≈ 1.5 kPa) for bone regeneration was observed. Similarly, the SN-GMO hydrogel formed by the Schiff base alone exhibited an insufficient

compression modulus (4.5 ± 0.7 kPa) with respect to achieving efficient bone repair. Therefore, in our study, the *in situ* reinforced hydrogel with double networks was achieved via the photopolymerization of GelMA. After visible light radiation, the mechanical strength of the DN-GMO hydrogel was significantly improved (Fig. 1F and G), which ensure a suitable micro-environment for osteogenesis.

Bioactive molecular delivery from bio-scaffold is a crucial strategy in bone tissue engineering [2]. Recently, a few self-healing and injectable hydrogels were reported to represent the promising outcomes in bone regeneration. For instance, Zhang et al. reported a self-healing hydrogel developed by crosslinking the oxidized dextran and adipic dihydrazide modified hyaluronic acid (HA) [53]. Accompanied with the LAP nanoplatelet-mediated BMP2 delivery, the nanocomposite hydrogels could greatly promote osteogenesis *in vitro* and *in vivo*. However, as to growth factors, the drawbacks such as high costs of production, immunogenicity and instability of are still needed to be overcome in clinical application. Utilizing inorganic materials, such as bioactive glass [54], may be an alternative choice. For example, Hou et al. prepared a biodegradable adhesive glue based on oxidized dextran and modified methacrylate gelatin for bone fracture fixation. The incorporation of aminated mesoporous bioactive glass nanoparticles (AMBGN) could further endow the hydrogel with the osteogenic activity [55]. However, more importance should be attached to angiogenesis process and vascular tissue formation during bone regeneration. To solve the problems above, peptides that can mimic the functions of osteogenic/angiogenic growth factors are worth exploring. BMP-2 has been reported to present a strong osteoinductive activity in numerous studies, so utilizing the peptides derived from the active BMP2 domain to promote the bone regeneration has attracted a significant attention recently [56,57]. Among these, the peptide corresponding to the residues 73–92, representing the knuckle epitope of the BMP2 protein, was observed to have the highest osteogenic activity by binding to the BMP receptor II on cells and initiating the BMP signal transduction [26]. As a crucial factor in vascular development and angiogenesis, VEGF played an important role in bone repair and bone regeneration [58,59]. Peptide based on the VEGF helix sequence had been proven to maintain the helix structure in liquid and demonstrate a high affinity to the kinase domain receptor (KDR), initiating the VEGF pathway transduction consequently [60]. Therefore, in our study, in order to achieve an efficient vascularized bone regeneration, the osteogenic peptide derived from BMP2 (knuckle epitope peptide, KP) and angiogenic peptide derived from VEGF (QK) were chose with slight modification. To minimize peptide structure alteration and avoid side reactions, only lysine in the N-terminal of peptide was kept in active state for subsequent chemical reaction.

Considering that the healing of the bone defect was a complex and long-term process [61], burst release of the bioactive molecules from bone grafting substitutes was obviously not satisfying. Although KP and QK were promising in vascularized bone regeneration due to their excellent osteogenic and angiogenic effect, a suitable releasing pattern from scaffold should be strived for. Physical adsorption was the simplest way to encapsulate bioactive factors into scaffolds [62]. However, weak interaction might result in burst release of bioactive factors, making it impossible to provide a sustained stimulation to target cells, which was especially important during bone tissue engineering. In contrast, the covalent bonds present a high bond energy and can provide a stable interaction between the bioactive factors and biomaterials [63], therefore, a reliable binding was achieved. However, such reactions require the additional catalysts or harsh conditions, which can complicate the process and may alter the biological functions of the binding factors. Moreover, too strong binding may give rise to immobilization of the factors, further impairing the cell recruitment and bone remodeling.

In the current study, taking into consideration the high content of aldehyde groups in the backbone of GMO hydrogel, two bioactive peptides (KP and QK) with active lysine in the N-terminus were stably tethered to the hydrogel matrix via Schiff base interaction. The reaction could be achieved by simply adding the peptides to pre-hydrogel

solution, without additional reagent. The sustained release profiles of both KP and QK from GMO hydrogel were observed, but QK showed a superior release kinetic than KP (Fig. 2H). It has been reported that KP has a β-strand like structure [26], while QK exhibits a helical structure [27]. As evidenced by the sequences and overall hydropathicity (GRAVY) analysis, QK showed a lower molecular weight and higher hydropathicity (GRAVY = −0.73) than KP (GRAVY = 0.39). Therefore, it was speculated that the difference in structures, length of sequence and hydropathicity of KP and QK might have contributed to the result. During physical bone healing, angiogenesis and osteogenesis occurred sequentially. The angiogenic factors, such as VEGF, were expressed at early stage to promote vascular tissue formation, while the osteogenic factors, such as BMP-2, come later for facilitating the bone tissue formation [15]. It has been reported that a controlled released of VEGF and BMP2 sequentially can promote the bone regeneration effectively [64]. As QK and KP mimic the corresponding functions of VEGF and BMP2, it was believed that the rapid-sustained release of QK and slow-sustained release of KP help to achieve a high efficient bone regeneration *in vivo*.

As shown, the KP and QK loaded GMO hydrogel exhibited strong osteogenic and angiogenic inductivities on BMSCs and HUVECs *in vitro*, respectively. The migration, proliferation and tube formation ability can reflect angiogenic potential of the endothelial cells [65]. The MAPK (ERK1/2) and PI3K/Akt signals, which can promote proliferation and migration during angiogenesis after activation, were the major downstream targets of VEGF pathway [58,66,67]. Besides, certain genes related to cell-cell interactions (such as *PECAM1*) and endothelial function (such as *PLVAP*, *VWF*) can indicate the angiogenic potential of endothelial cells as well [68]. In our study, GMO hydrogel loaded with QK significantly enhanced migration, proliferation and tube formation by activating the angiogenesis related pathways as well as stimulating the expression of the angiogenic genes of HUVECs, indicating great angiogenic induction potential. These results were consistent with the earlier reports of the QK modified scaffold materials showing a vast improvement in angiogenesis *in vitro* [69–71]. The osteogenic differentiation of BMSCs could be reflected by the high expression of the osteogenic genes, increased alkaline phosphatase activity and elevated production of the bone-like calcium deposits. GMO hydrogel loaded with KP demonstrated a significantly promoted osteogenesis, which were consistent with previous studies about other BMP-2 derived peptide modified scaffold materials [72–74].

As shown in Figs. 6 and 7, consistent with the *in vitro* results, GMO hydrogel loaded with KP showed a significant enhancement of bone regeneration *in vivo*. This further verified the osteoinductivity of KP in GMO hydrogels. Interestingly, although QK demonstrated a limited effect on the osteogenic differentiation of BMSCs *in vitro*, the QK incorporated GMO hydrogel showed a slight promotion of the bone formation *in vivo*. Considering increased angiogenesis by QK *in vitro*, our result was consistent with previous studies indicating that the angiogenesis process induced by VEGF could further promote osteogenesis *in vivo* [58,75]. Moreover, a synergistic effect of QK and KP *in vivo* was observed in this study as the GMO hydrogel loaded with both KP and QK showed the highest healing efficiency of bone defect among all groups. It is widely known that angiogenesis and osteogenesis are independent in bone regeneration process. The increased vascular tissue formation induced by QK can further provide sufficient nutrition and more osteogenesis bioactive factors for maturity of MSCs, whereas the angiogenic bioactive factors secreted by osteocytes in turn strengthen the angiogenesis process [15,64]. It was likely that these independent processes finally led to the synergistic effects and superior bone tissue restoration.

In the past decades, the bone tissue engineering strategy of employing the bioactive factors and/or exogenous stem cells to fill the defects area, has achieved excellent advancements in bone repair [4]. However, deliver of exogenous stem cells suffered from increasing limitations such as low acquiring ratio, low survival rates, impaired therapeutic efficacy, risk of rejection and immunological reactions [76]. Considering the recruiting ability of bioactive peptides, a cell-free

strategy was chosen in this study. Released peptides from the hydrogel could initiate angiogenesis and recruit sufficient stem cells from the microenvironment. Subsequently, osteogenic was stimulated, leading to an efficient bone regeneration afterwards. The current results indicated that delivering KP and QK together in GMO hydrogel could achieve an efficient bone regeneration *in vivo*.

The present study also had several limitations. First, only BMSCs and HUVECs were used to investigate the osteogenic and angiogenic inductivities of KP and QK. For the sake of intricate microenvironment and network of bone regeneration, multiple cell types should be included in future studies. Second, though the two functional peptides showed a sustained released profile from the GMO hydrogel, however, the mechanism of the releasing activity need to further explored. As to the GMO hydrogel, developing new strategy to deliver functional peptides in a more spatio-temperally controllable way is worth exploring. Third, in this study, we only adopted the cell-free material strategy with bioactive peptides. In fact, the GMO hydrogel also has tremendous potential as a cell-laden injectable scaffold. In GMO hydrogel, the broken dynamic covalent bonds during injection might disperse the harmful forces and protect encapsulated cells from mechanical injuries, therefore, enhancing the cell survival and stem cell abased bone tissue engineering. In the future, it is worth investigating the suitable cell-laden strategies for bone regeneration based on GMO hydrogel. Finally, though the GMO hydrogel displayed a significant potential as a minimally invasive and efficient approach for bone defect repair, the detailed protocols for clinical application, such as about injection and photo-reinforcement, need to be further explored and optimized. Inspired by the arthroscopic device used to inject and photocrosslink hydrogel for articular cartilage repair [77], similar minimally invasive (MIS) devices may be a solution for GMO hydrogels application in practice.

5. Conclusion

A novel injectable and self-healing hydrogel (GMO), loaded with both osteogenic and angiogenic peptides, was developed in this study for efficient bone regeneration. This composite GMO hydrogel exhibited high biocompatibility, desirable mechanical strength, excellent injectable and self-healing abilities, which guaranteed a minimally invasive and convenient approach for irregular and small bone defects restoration. Two bioactive peptides (KP and QK), derived from BMP2 and VEGF, were tethered to the GMO hydrogel via the Schiff base bond and achieved the desirable releasing profiles. *In vitro*, the KP and QK loaded GMO hydrogel not only increased the expression of the osteogenic genes, alkaline phosphatase activities and production of the bone-like calcium deposits of BMSCs, but also promoted the proliferation, migration, tube formation ability and angiogenic signaling transduction of HUVECs. *In vivo*, the GMO hydrogel loaded with KP and QK revealed a significant synergistic promotion of both osteogenesis and angiogenesis, thus, resulting in a markedly enhanced bone formation in the rat calvaria defect. Overall, the KP/QK loaded into GMO hydrogel was proven to serve as an efficient approach for the vascularized bone regeneration, providing an injectable self-healing material and suggesting a new strategy for bone tissue engineering via a minimally invasive approach.

CRediT authorship contribution statement

Runze Li: Conceptualization, Methodology, Formal analysis, Writing – original draft. **Chen Zhou:** Methodology, Formal analysis, Writing – original draft. **Jun Chen:** Conceptualization, Formal analysis, Writing – original draft. **Haotian Luo:** Investigation. **Ruoyu Li:** Investigation. **Danyin Chen:** Data curation. **Xuenong Zou:** Conceptualization, Writing – review & editing. **Weicai Wang:** Supervision, Validation, Writing – review & editing.

Declaration of competing interest

The authors declare no conflict of interest.

Acknowledgements

Appendix A. Supplementary data

Supplementary data to this article can be found online at https://doi.org/10.1016/j.bioactmat.2022.02.011.

References

[1] N.L. Fazzalari, Bone fracture and bone fracture repair[J], Osteoporos. Int. J Established Result Cooperation Eur. Found. Osteopor. Nat. Osteoporosis Found. USA 22 (6) (2011) 2003–2006.

[2] Ho-Shui-Ling Antalya, Bolander Johanna, E. Rustom Laurence, et al., Bone regeneration strategies: engineered scaffolds, bioactive molecules and stem cells current stage and future perspectives[J], Biomaterials 180 (2018) 143–162.

[3] R. Tevlin, A. McArdle, D. Atashroo, et al., Biomaterials for craniofacial bone engineering[J], J. Dent. Res. 93 (12) (2014) 1187–1195.

[4] L. Koons Gerry, Diba Mani, G. Mikos Antonios, Materials design for bone-tissue engineering[J], Nat. Rev. Mater. 5 (8) (2020) 584–603.

[5] Bai Xin, Mingzhu Gao, Sahla Syed, et al., Bioactive hydrogels for bone regeneration [J], Bioactive Materials 3 (4) (2018) 401–417.

[6] Raucci Maria Grazia, D'Amora Ugo, Ronca Alfredo, et al., Injectable functional biomaterials for minimally invasive surgery[J], Advanced Healthcare Materials 9 (13) (2020), e2000349.

[7] Liow Sing Shy, Qingqing Dou, Kai Dan, et al., Thermogels: in situ gelling biomaterial[J], ACS Biomater. Sci. Eng. 2 (3) (2016) 295–316.

[8] S. Stilhano Roberta, L. Madrigal Justin, Kevin Wong, et al., Injectable alginate hydrogel for enhanced spatiotemporal control of lentivector delivery in murine skeletal muscle[J], J. Contr. Release 237 (2016) 42–49.

[9] R. Jin, L.S. Moreira Teixeira, P.J. Dijkstra, et al., Enzymatically-crosslinked injectable hydrogels based on biomimetic dextran–hyaluronic acid conjugates for cartilage tissue engineering[J], Biomaterials 31 (11) (2010) 3103–3113.

[10] L. Ifkovits Jamie, A. Burdick Jason, Review: photopolymerizable and degradable biomaterials for tissue engineering applications[J], Tissue Eng. 13 (10) (2007) 2369–2385.

[11] Zongrui Tong, Lulu Jin, Joaquim Miguel Oliveira, et al., Adaptable hydrogel with reversible linkages for regenerative medicine: dynamic mechanical microenvironment for cells[J], Bioactive Materials 6 (5) (2021) 1375–1387.

[12] Chunxiang Mo, Li Xiang, Yuping Chen, Advances in injectable and self-healing polysaccharide hydrogel based on the Schiff base reaction[J], Macromol. Rapid Commun. 42 (10) (2021), e2100025.

[13] Saravanan Sekaran, Vimalraj Selvaraj, Thanikaivelan Palanisamy, et al., A review on injectable chitosan/beta glycerophosphate hydrogels for bone tissue regeneration[J], Int. J. Biol. Macromol. 121 (2019) 38–54.

[14] Yujie Tu, Nuan Chen, Chuping Li, et al., Advances in injectable self-healing biomedical hydrogels[J], Acta Biomater. 90 (2019) 1–20.

[15] Diomede Francesca, Marconi Guya Diletta, Fonticoli Luigia, et al., Functional relationship between osteogenesis and angiogenesis in tissue regeneration[J], Int. J. Mol. Sci. 21 (9) (2020) E3242.

[16] S. Salazar Valerie, W. Gamer Laura, Vicki Rosen, BMP signalling in skeletal development, disease and repair[J], Nat. Rev. Endocrinol. 12 (4) (2016) 203–221.

[17] K.D. Hankenson, K. Gagne, M. Shaughnessy, Extracellular signaling molecules to promote fracture healing and bone regeneration[J], Adv. Drug Deliv. Rev. 94 (2015) 3–12.

[18] Yong Wu, Tianqi Chang, Weiqian Chen, et al., Release of VEGF and BMP9 from injectable alginate based composite hydrogel for treatment of myocardial infarction[J], Bioactive Materials 6 (2) (2021) 520–528.

[19] Shangsi Chen, Yufei Shi, Xin Zhang, et al., Evaluation of BMP-2 and VEGF loaded 3D printed hydroxyapatite composite scaffolds with enhanced osteogenic capacity in vitro and in vivo[J], Mater. Sci. Eng. C 112 (2020), 110893.

[20] Qiang Wang, Yanxia Zhang, Bin Li, et al., Controlled dual delivery of low doses of BMP-2 and VEGF in a silk fibroin–nanohydroxyapatite scaffold for vascularized bone regeneration[J], J. Mater. Chem. B 5 (33) (2017) 6963–6972.

[21] W. James Aaron, LaChaud Gregory, Jia Shen, et al., A review of the clinical side effects of bone morphogenetic protein-2[J]. Tissue engineering, Part B, Reviews 22 (4) (2016) 284–297.

[22] C. Mitchell Aaron, S. Briquez Priscilla, A. Hubbell Jeffrey, et al., Engineering growth factors for regenerative medicine applications[J], Acta Biomater. 30 (2016) 1–12.

[23] Andy Chi-Lung Lee, Janelle Louise Harris, Kum Kum Khanna, et al., A comprehensive review on current advances in peptide drug development and design[J], Int. J. Mol. Sci. 20 (10) (2019) E2383.

[24] Lian Zheng, Tianjiao Ji, Functional peptide-based drug delivery systems[J], J. Mater. Chem. B 8 (31) (2020) 6517–6529.

[25] Jie Liao, Shuai Wu, Li Kun, et al., Peptide-modified bone repair materials: factors influencing osteogenic activity[J], J. Biomed. Mater. Res. 107 (7) (2019) 1491–1512.

[26] Wei Zhang, Jiazhi Liu, Haojie Shan, et al., Machine learning-guided evolution of BMP-2 knuckle Epitope-Derived osteogenic peptides to target BMP receptor II[J], J. Drug Target. (2020) 1–9, 0(0).

[27] Finetti Federica, Basile Anna, Capasso Domenica, et al., Functional and pharmacological characterization of a VEGF mimetic peptide on reparative angiogenesis[J], Biochem. Pharmacol. 84 (3) (2012) 303–311.

[28] Lihui Weng, Xuming Chen, Weiliam Chen, Rheological characterization of in situ crosslinkable hydrogels formulated from oxidized dextran and N-carboxyethyl chitosan[J], Biomacromolecules 8 (4) (2007) 1109–1115.

[29] Soleimani Masoud, Nadri Samad, A protocol for isolation and culture of mesenchymal stem cells from mouse bone marrow[J], Nat. Protoc. 4 (1) (2009) 102–106.

[30] K. Nemeth, B. Mayer, B.J. Sworder, et al., A practical guide to culturing mouse and human bone marrow stromal cells[J], Curr. Protoc. Im. 102 (1) (2013) 22F.12.1–22F.12.13.

[31] Meena Lalit Kumar, Raval Pavani, Kedaria Dhaval, et al., Study of locust bean gum reinforced cyst-chitosan and oxidized dextran based semi-IPN cryogel dressing for hemostatic application[J], Bioactive Materials 3 (3) (2018) 370–384.

[32] Fushan Hou, Wei Jiang, Yin Zhang, et al., Functional and pharmacological characterization of a VEGF mimetic peptide on reparative angiogenesis[J], Chem. Eng. J. 427 (2022), 132000.

[33] Xin Zhao, Li Peng, Baolin Guo, et al., Antibacterial and conductive injectable hydrogels based on quaternized chitosan-graft-polyaniline/oxidized dextran for tissue engineering[J], Acta Biomater. 26 (2015) 236–248.

[34] Aldana Ana Agustina, Malatto Laura, Rehman Muhammad Atiq Ur, et al., Fabrication of gelatin methacrylate (GelMA) scaffolds with nano- and micro-topographical and morphological features, J. Nanomater. 9 (1) (2019) 120.

[35] Lien Sio-Mei, Liang-Yu Ko, Ta-Jen Huang, Effect of pore size on ECM secretion and cell growth in gelatin scaffold for articular cartilage tissue engineering[J], Acta Biomater. 5 (2) (2009) 670–679.

[36] N. Kelly Cambre, Tian Wang, Crowley James, et al., High-strength, porous additively manufactured implants with optimized mechanical osseointegration[J], Biomaterials 279 (2021), 121206.

[37] Xiaoya Ding, Ye Wang, Jiaying Liu, et al., Injectable in situ forming double-network hydrogel to enhance transplanted cell viability and retention[J], Chem. Mater. 33 (15) (2021) 5885–5895.

[38] Juan Ma, Anyi Guo, Shunhao Wang, et al., From the lung to the knee joint: toxicity evaluation of carbon black nanoparticles on macrophages and chondrocytes[J], J. Hazard Mater. 353 (2018) 329–339.

[39] Juan Ma, Ruibin Li, Liu Yin, et al., Carbon nanotubes disrupt iron homeostasis and induce anemia of inflammation through inflammatory pathway as a secondary effect distant to their portal-of-entry[J], Small 13 (15) (2017).

[40] S. Apte Rajendra, S. Chen Daniel, Napoleone Ferrara, VEGF in signaling and disease: beyond discovery and development[J], Cell 176 (6) (2019) 1248–1264.

[41] Zeming Gu, Jianzhong Fu, Lin Hui, et al., Development of 3D bioprinting: from printing methods to biomedical applications[J], Asian J. Pharm. Sci. 15 (5) (2020) 529–557.

[42] Shen Chen, Witek Lukasz, L. Flores Roberto, et al., Three-dimensional printing for craniofacial bone tissue engineering[J], Tissue Eng. 26 (23–24) (2020) 1303–1311.

[43] Jiayu Liu, Hongli Zeng, Peng Xiao, et al., Sustained release of magnesium ions mediated by a dynamic mechanical hydrogel to enhance BMSC proliferation and differentiation[J], ACS Omega 5 (38) (2020) 24477–24486.

[44] Bo Jiang, Jian Yang, Rahoui Nahla, et al., Functional polymer materials affecting cell attachment[J], Adv. Colloid Interface Sci. 250 (2017) 185–194.

[45] Luanluan Jia, Fengxuan Han, Huan Wang, et al., Polydopamine-assisted surface modification for orthopaedic implants[J], Journal of Orthopaedic Translation 17 (2019) 82–95.

[46] L. Segura José, J. Mancheño María, Félix Zamora, Covalent organic frameworks based on Schiff-base chemistry: synthesis, properties and potential applications[J], Chem. Soc. Rev. 45 (20) (2016) 5635–5671.

[47] Kan Yue, Santiago Grissel Trujillo-de, Moisés Alvarez Mario, et al., Synthesis, properties, and biomedical applications of gelatin methacryloyl (GelMA) hydrogels [J], Biomaterials 73 (2015) 254–271.

[48] Xuan Zhao, Saiqun Li, Xinyue Du, et al., Natural polymer-derived photocurable bioadhesive hydrogels for sutureless keratoplasty[J], Bioactive Materials 8 (2022) 196–209.

[49] Yunsong Shi, Ruijun He, Xiangyu Deng, et al., Three-dimensional biofabrication of an aragonite-enriched self-hardening bone graft substitute and assessment of its osteogenicity in vitro and in vivo[J], Biomaterials Translational 1 (1) (2020) 69.

[50] Hongjie Zhang, Qiuquan Cai, Yanhui Zhu, et al., A simple hydrogel scaffold with injectability, adhesivity and osteogenic activity for bone regeneration[J], Biomaterials Science 9 (3) (2021) 960–972.

[51] Zandi Nooshin, Sani Ehsan Shirzaei, Mostafavi Ebrahim, et al., Nanoengineered shear-thinning and bioprintable hydrogel as a versatile platform for biomedical applications[J], Biomaterials 267 (2021), 120476.

[52] Tseng Ting-Chen, Tao Lei, Fu-Yu Hsieh, et al., An injectable, self-healing hydrogel to repair the central nervous system[J], Advanced Materials (Deerfield Beach, Fla.) 27 (23) (2015) 3518–3524.

[53] Yuanhao Zhang, Mingjiao Chen, Zhaobo Dai, et al., Sustained protein therapeutics enabled by self-healing nanocomposite hydrogels for non-invasive bone regeneration[J], Biomaterials Science 8 (2) (2020) 682–693.

[54] Fujian Zhao, Zhen Yang, Liu Lu, et al., Design and evaluation of a novel sub-scaffold dental implant system based on the osteoinduction of micro-nano bioactive glass[J], Biomaterials Translational 1 (1) (2020) 82.

[55] Fushan Hou, Wei Jiang, Yin Zhang, et al., Biodegradable dual-crosslinked adhesive glue for fixation and promotion of osteogenesis[J], Chem. Eng. J. 427 (2022), 132000.

[56] Visser Rick, A. Rico-Llanos Gustavo, Pulkkinen Hertta, et al., Peptides for bone tissue engineering[J], J. Contr. Release 244 (2016) 122–135.

[57] Jabbari Esmaiel, Osteogenic peptides in bone regeneration[J], Curr. Pharmaceut. Des. 19 (19) (2013) 3391–3402.

[58] Kai Hu, R. Olsen Bjorn, The roles of vascular endothelial growth factor in bone repair and regeneration[J], Bone 91 (2016) 30–38.

[59] Yong Liu, Jiarui Fang, Quan Zhang, et al., Wnt10b-overexpressing umbilical cord mesenchymal stem cells promote critical size rat calvarial defect healing by enhanced osteogenesis and VEGF-mediated angiogenesis[J], Journal of Orthopaedic Translation 23 (2020) 29–37.

[60] L.D. D'Andrea, G. Iaccarino, R. Fattorusso, et al., Targeting angiogenesis: structural characterization and biological properties of a de novo engineered VEGF mimicking peptide[J], Proc. Natl. Acad. Sci. Unit. States Am. 102 (40) (2005) 14215–14220.

[61] A. Einhorn Thomas, C. Gerstenfeld Louis, Fracture healing: mechanisms and interventions[J], Nat. Rev. Rheumatol. 11 (1) (2015) 45–54.

[62] Yuze Zeng, Hoque Jiaul, Shyni Varghese, Biomaterial-assisted local and systemic delivery of bioactive agents for bone repair[J], Acta Biomater. 93 (2019) 152–168.

[63] Jingjing Luo, Haitao Zhang, zhu Jiang, et al., 3-D mineralized silk fibroin/polycaprolactone composite scaffold modified with polyglutamate conjugated with BMP-2 peptide for bone tissue engineering[J], Colloids Surf. B Biointerfaces 163 (2018) 369–378.

[64] S. Lee Seunghun, Kim Jung Hun, Jiwoon Jeong, et al., Sequential growth factor releasing double cryogel system for enhanced bone regeneration[J], Biomaterials 257 (2020), 120223.

[65] Lamalice Laurent, Boeuf Fabrice Le, Huot Jacques, Endothelial cell migration during angiogenesis[J], Circ. Res. 100 (6) (2007) 782–794.

[66] R. Muñoz-Chápuli, A.R. Quesada, M. Ángel Medina, Angiogenesis and signal transduction in endothelial cells[J], Cellular Mol. Life Sci. CMLS 61 (17) (2004) 2224–2243.

[67] Bing-Hua Jiang, Liu Ling-Zhi, AKT signaling in regulating angiogenesis[J], Curr. Cancer Drug Targets 8 (1) (2008) 19–26.

[68] Jimmy Su, C. Satchell Simon, A. Wertheim Jason, et al., Poly(ethylene glycol)-crosslinked gelatin hydrogel substrates with conjugated bioactive peptides influence endothelial cell behavior[J], Biomaterials 201 (2019) 99–112.

[69] Amrita Pal, I. Smith Cameron, Palade Joanna, et al. Poly(N-isopropylacrylamide)-based dual-crosslinking biohybrid injectable hydrogels for vascularization[J], Acta Biomater. 107 (2020) 138–151.

[70] W. Pensa Nicholas, S. Curry Andrew, S. Reddy Michael, et al., Sustained delivery of the angiogenic QK peptide through the use of polyglutamate domains to control peptide release from bone graft materials[J], J. Biomed. Mater. Res. 107 (12) (2019) 2764–2773.

[71] Daniel A. Young, B. Pimentel Marja, Lima Luana Dias, et al., Design and characterization of hydrogel nanoparticles with tunable network characteristics for sustained release of a VEGF-mimetic peptide[J], Biomaterials Science 5 (10) (2017) 2079–2092.

[72] Seung Hun Park, Park Joon Yeong, Ji Yun Bae, et al., An injectable click-crosslinked hyaluronic acid hydrogel modified with a BMP-2 mimetic peptide as a bone tissue engineering scaffold[J], Acta Biomater. 117 (2020) 108–120.

[73] Mun-Jung Kim, Bora Lee, Kisuk Yang, et al., BMP-2 peptide-functionalized nanopatterned substrates for enhanced osteogenic differentiation of human mesenchymal stem cells[J], Biomaterials 34 (30) (2013) 7236–7246.

[74] Ang Li, Li Jian, Zhengye Zhang, et al., Nanohydroxyapatite/polyamide 66 crosslinked with QK and BMP-2-derived peptide prevented femur nonunion in rats [J], J. Mater. Chem. B 9 (9) (2021) 2249–2265.

[75] Shuang Zhang, Jie Chen, Yuanman Yu, et al., Accelerated bone regenerative efficiency by regulating sequential release of BMP-2 and VEGF and synergism with sulfated chitosan[J], ACS Biomater. Sci. Eng. 5 (4) (2019) 1944–1955.

[76] Li Li, Hongwei Lu, Yulan Zhao, et al., Functionalized cell-free scaffolds for bone defect repair inspired by self-healing of bone fractures: a review and new perspectives[J], Mater. Sci. Eng. C 98 (2019) 1241–1251.

[77] Yujie Hua, Huitang Xia, Litao Jia, et al., Ultrafast, tough, and adhesive hydrogel based on hybrid photocrosslinking for articular cartilage repair in water-filled arthroscopy[J], Sci. Adv. 7 (35) (2021), eabg0628.